PONTIFICIA UNIVERSIDAD CATÓLICA DEL PERÚ

ESCUELA DE POSGRADO

The study of backgrounds and the incoherent contribution for neutrino trident production

A thesis submitted for the degree of Master of Science in Physics

Jose Antonio Becerra Aguilar

Advisor

Gago Medina, Alberto Martin

Lima, Perú
June 13, 2018

Abstract

We studied dimuon events arising from trident production, for both coherent and incoherent processes, as well as relevant backgrounds, in order to predict the number of expected events observed in the lifetimes of current and forthcoming neutrino experiments. In particular, for this thesis, we focused in building the implementation of the incoherent contribution within the context of the GENIE montecarlo generator. We also developed relatively detailed GEANT4 geometries for the MINERvA detector as well as the DUNE Near Detector, for the Liquid Argon (LArTPC) and Straw Tube Tracker (STT) proposals. A very careful study of the backgrounds for the incoherent case was carried, in order to complement the study already done for the coherent contribution. Then, we combined the signals for the coherent and incoherent processes to realize a more realistic study of the expected number of events. The ROOT TMVA package for multivariate analysis was then used to filter signal from background. The results are presented in terms of number of events, and are calibrated based on the detector exposure in the lifetime of the MINERvA detector and DUNE Near Detector.

Aknowledgements

I would like to thank the *Cienciactiva* initiative from the *Consejo Nacional de Ciencia Tecnología e Innovación Tecnológica (CONCYTEC)* for their financing of my Master's degree studies, without which this workcould not have been possible. Iwould also like to thank my advisor Alberto Gago, for his leadership in organizing the efforts from all participants along these twoyears of investigation. Moreover, I would also like to give my thanks to Sebastian Sanchez for his constant guidance, as well as his hard work on the development of the implementation of the trident interaction in GENIE, and also to Eric Endress, for without his theoretical and computational calculations of the trident cross section, this investigation would not have been possible. Finally I would also like to thank my father, for his love and support. He has always encouraged me without hesitation to follow my dreams and accomplish my goals, and I would not be the person I am today without him.

Contents

Introduction

The neutrino (ν) is a type of elementary particle that has no electric charge and only interacts with matter through gravity and the weak force. It is also a fermion, since it has non-integer spin (1/2), and can belong to one of three types (flavors): the electron (ν_e), muon (ν_μ) and tau (ν_τ) neutrinos. The study of the physical properties of the neutrino has been a prominent area of research for high energy physics in the past decades, as the study of its peculiar properties has helped us havea better understanding of the way the universe works. This was the case even as early as the first time it was postulated by Wolgang Pauli in 1930 in order to explain the lack of conservation of momentum in beta decay. It was later finally detected in 1956, at which time it was thought to be a massless particle. This wasthen put into question, as the phenomenom of neutrino flavor oscillation was observed. The flavor oscillation phenomenom occurs because the three neutrino flavors do not line up perfecty with the three masses that a neutrino can have, resulting in each mass state being a superposition of flavor states. Neutrinos have also been a useful tool for acquiring information from celestial bodies. Since neutrinos rarely interact, they can travel long distances through the vacuum of space, making it possible to study the spectra of neutrinos produced at distant stars, galaxies or even supernovae. Finally sterile neutrinos have also become a strong candidate for dark matter.

This increased interest in the effective detection and understanding of the way neutrinos interact with matter has fueled the construction ofvarious neutrino experiments like NuTeV, CHARM II, and in more recent years MINERνA and MicroBooNE, which have concentrated in the development of neutrino detection technologies as well as cross-section measurements. There have also been experiments built exclusively for the detection and measurement of parameters related to neutirino oscillation, like the MINOS[1] experiment at Fermilab, as well as the K2K experiment in Japan[2].

Neutrino Interactions In the medium energy range, between 0.1 and 20 GeV approximately, which is the range of energy at which our investigation will take place, neutrino interactions are normally divided into regimes, depending on the energy of the incident neutrino. The reason for this, is that the higher the energy of the incident

neutrino, the more in depth it can probe the internal structure of the nucleons (protons, neutrons) it interacts with. Therefore, it is common practice to speak of three different interaction regimes: The quasi-elastic (QEL), the resonant scattering (RES), and the deep inelastic scattering (DIS) regimes.

In the quasi-elastic regime, the neutrino interacts with individual nucleons and not with its constituent partons (quarks, gluons). It is caracterized by not having a hadronic shower, but instead producing a lepton and a nucleon in the final state, since it is a charged current (CC) interaction. If the incident particle is a neutrino (ν), then the struck neutron becomes a proton and the neutrino becomes its corresponding lepton of the same flavor, if instead the incident particle is an antineutrino ($\bar{\nu}$), the struck neutron becomes a proton and the neutrino becomes its correspondingo antilepton. In the resonant regime, the incident neutrino has an energy that is high enough to produce a baryon resonance when striking the target nucleon, usually in the way of single pion production. Finally the last regime is the deep inelastic regime, in which the neutrino interacts with the individual partons composing the struck nucleon. This scattering is usually caracterized by a high momentum transfer between the neutrino and the target nucleon, resulting in a hadronic shower. Figure 1 shows the total cross section for neutrino interactions and how it divides into the three regimes described above.

Apart from the three regimes described above, a fourth type pf classification that is relevant for this investigation are the coherent interactions. These interactions can be observed at a wide range of energies, thus they do not fall into a specific regime, like the ones described above. Coherent interactions are characterized by having a low momentum transfer between the neutrino and the target nucleus, and as a result, do not interact directly with its constituent nucleons. Instead the neutrino interacts with ne nucleus as a whole and nucleons are not expelled from the nucleus in the final state. Having made the relevantdistinctions between the ways neutrinos interact with matter, this paper focuses on the study of a specific type of neutrino interaction, called *trident production*.

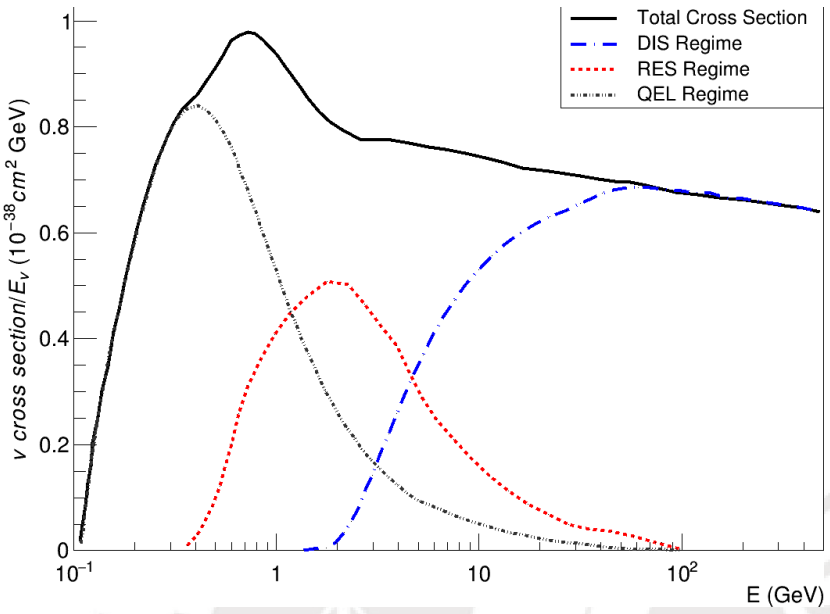

Figure 1: Different regimes for the neutrino cross section. The graphs are based on the plots in reference [3]

Trident Production Trident production is the name given to the interaction in which a neutrino scatters off the Coulomb field in an atom, producing another neutrino and a lepton-antilepton pair. Although theoretically trident production can produce a pair of leptons of different flavors, this paper focuses on the case where a μ - μ^+ pair is produced.

$$\nu_\mu + N \rightarrow \nu_\mu + \mu^+ + \mu^- \tag{1}$$

There is newfound interest in the study of this process because of its potential for studying extensions of the standard model (SM) in the form of new neutral current (NC) bosons, an example being the study of NC bosons coupled to a L_μ L_τ symmetry [4]. The presence of these new Z' bosons is expected to be observable due to the interference they would have with their SM counterparts. As a result, we could take advantage of current and future neutrino experiments, like MINERνA detector, or the future DUNE experiment at the LBNF at Fermilab, to measure the deviation in the number of observed trident events from the SM predictions.

One big obstacle in investigation trident production, however, is its small cross section, which can be between 4 and 6 orders of magnitude smaller than the charged

current (CC) one, as it is shown in figure 2. This small cross section, combined with the the energy limitations in current and upcoming neutrino beam experiments2.5, make it difficult to study, due to the small number of events that could be expected in an experiment's lifetime[5]. Furthermore, there are papers, like reference [6] that suggest background contributions may be many times larger than the trident signal itself. This puts greater importance in works that study the kinematical distributions of the $\mu\mu^+$ pair that is produced[7], which could be really helpful when trying to separate trident events from their background. Given the importance of this distinction, this paper focuses on the simulation of the trident signal and its most important backgrounds, with the aim of feeding the kinematic distributions of the final state particles into the ROOT's TMVA package[8] for multivariate analysis in order to filter signal from background, as described in section 2.5.

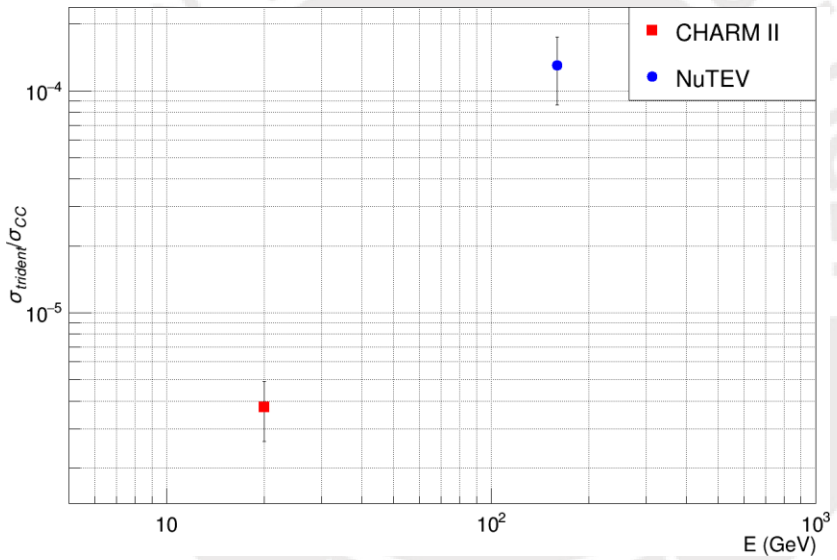

Figure 2: Both measurements of the trident cross-section, as measured by the CHARM II[9] and NuTeV[10] experiments, shown as a ratio between the total trident cross-section and the inclusive CC cross section.

Dissertation outline

Following this introduction, the first chapter focuses on the theoretical aspects of our signal and background. It starts by describing the two trident processes that we are going to study, the coherent and the incoherent one. Then, we proceed to cover the calculation of the cross-section being studied, starting from the Feynman diagrams, with the aim of reproducing the calculations made by [11] in the context of a V-

A theory. This would allow us to add the C_V and C_A coupling constants that are be responsible for the interference of the $W^{\pm}$ and Z^0 bosons in the SM. The capter continues to explain in greater detail the different parametrizations for the nuclear forms factor, as well as nuclear charge densities that have been taken into account, in order to see the magnitude of their effect on the cross section. Finally the chapter ends by describing the three background processes that we are taking into account. In the third chapter, we start by describing the experimental setups of the MINERνA and DUNE Near Detectors, proceed by defining the experimental observables that we have taken into account for our analysis, and end it by explaining the methodology used for our analysis with the ROOT TMVA package. Finally, the fourth chapter shows the results from the TMVA analysis and the discussion about what they imply regarding the feasibility ofstudying trident interactions in MIVERνA-like and DUNE-like experiments.

Chapter 1

Theoretical Aspects

1.1 The four fundamental forces

All interactions between particles can be linked to one of the four fundamental forces, which are described in table 1.1, moreover, the interaction between two particles through a given force is always accompanied by a *mediator boson*. The *strong force* is a fundamental interaction mediated by *gluons* (g) that affects hadrons, which are the particles that are made up of quarks. The *electromagnetic force* affects all particles that posses an electric charge and is mediated by the *photon* (γ). The *weak force* affects all fermions, that is, particles with a non-integer spin, and is responsible for radioactive decay. It is mediated by the Z^0 and $W^{\pm}$ bosons. Finally, the *gravitational force* affects light and all particles that possess mass. There is yet to be found a physical theory that can both describe satisfactorily the effect of gravity at quantum level and be proven by present day experiments, therefore its mediator is not part of the standard model. However, if it were to exist, its would be called the *graviton*.

A way to probe the physical properties of these particles and the forces that govern their interactions is by looking at how they interact with matter through *scattering* experiments.

Force	Strong	Electromagnetic	Weak	Gravitational
Theory	Chromodynamics	Electrodynamics	Flavordynamics	General relativity
Mediator	Gluon (g)	Photon (γ)	$W^{\pm}$ and Z^0 bosons	Graviton

Table 1.1: The four elementary forces and their corresponding mediator particles.

Quarks	up	charm	top
	down	strange	bottom
Leptons	e	μ	τ
	ν_e	ν_μ	ν_τ
Mediator Bosons	γ	Z^0, $W^\pm$	g

Table 1.2: Elementary particles of the standard model. In the first two rows are the six quarks. In the next two rows we see the three families of charged leptons (e, μ and τ) and their corresponding neutrinos. Finally, the last row shows the mediator bosons for the strong, weak and electromagnetic forces.

1.1.1 The weak force

As mentioned in the introduction, trident production is one of the many processes a neutrino can go through when it interacts with matter. We also mentioned that neutrinos interact with matter mainly through the weak force. As mentioned earlier in this chapter, the weak force acts upon fermions (leptons and quarks) and is mediated by two propagators, the $W^\pm$ and Z^0 bosons. The weak force is the only force able to change neutrinos into their corresponding leptons i.e. an electron (e) can be changed into an electron neutrino (ν_e), a muon (μ)into a muon neutrino (ν_μ) and a tau (τ) into a tau neutrino (ν_τ). These changes between leptons of the same "flavor" are mediated by the W^+ boson, as it is shown in the right diagram on figure1.1.

$$\frac{-ig}{2\sqrt{2}}\gamma^\mu(1-\gamma^5) \quad \mu = 0, 1, 2, 3 \tag{1.1}$$

This construction of the CC current is said to be *vector-axial vector* (V-A), because when the vertex term above is combined with the $u(p)$ spinors to form thecurrent term, it ends up having a vector component ($\bar{u}_f\gamma^\mu u_i$) as well as an vector-axial one ($\bar{u}_f\gamma^\mu\gamma^5 u_i$). The $\bar{u}_f\gamma^\mu u_i$ term is denoted as a vector, because it has four components and under the inversion of coordinates (parity operation P) it changes to: $P^{-1}\bar{u}_f\gamma^\mu u_i P = \bar{u}_f\gamma^{\mu\dagger}u_i$. Where $\gamma^{\mu\dagger}$ differs from γ^μ only in that it acquires aminus sign in its spacial components ($\mu = 1, 2, 3$). In a similar fashion, the $\bar{u}_f\gamma^\mu\gamma^5 u_i$ term also has four components, but does not vary under a parity operation, $P^{-1}\bar{u}_f\gamma^\mu\gamma^5 u_i P = \bar{u}_f\gamma^\mu\gamma^5 u_i$, and is thus called an axial-vector.

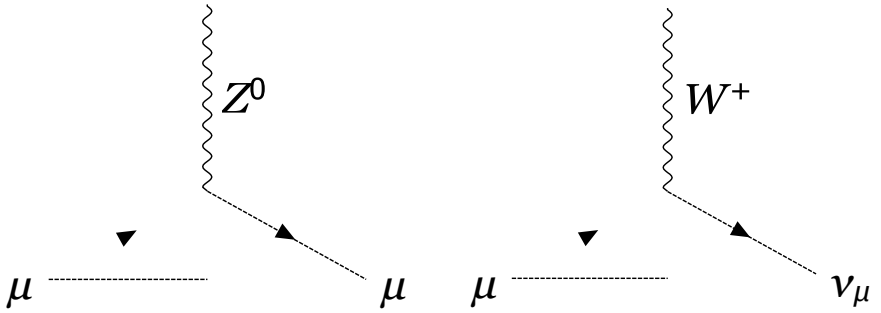

Figure 1.1: Charged current (CC) and neutral current (NC) fundamental vertices.

Weak interactions can also be mediated by a neutral boson Z^0. In this case the interaction vertex is not perfectly balanced between the axial-vector and vector components. Instead, it contains the C_V and C_A couplings which, depending on the interaction, give a greater importance to the vector or axial-vector terms.

$$\frac{-ig_z}{2}\gamma^\mu(C_V - C_A\gamma^5) \tag{1.2}$$

1.2 The Trident Production Process

Based on the different regimes describes in section , we recognize the existence of three regimes for trident production, depending on the valueof the q^2 tranfered: First, in the coherent regime, at low Q^2 values, neutrinos can interact with the nucleus as a whole. At intermediate Q^2 values we encounter the incoherent regime, where neutrinos are able to interact directly with individual nucleons. Finally, for high Q^2 values, we find the DIS regime, where they are able to interact directly with quarks. In this paper, we study the coherent and incoherent cases, ilustrated in Figure 1.4.

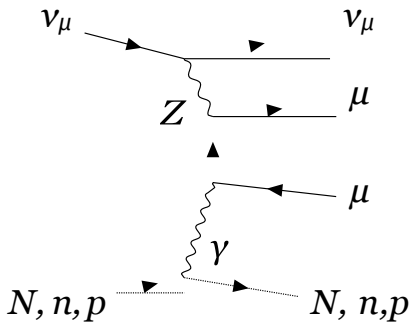

Figure 1.2: Example of one of the possible Feynmann diagrams for trident production. It can be seen that the diagram is valid for neutrinos scattering off either a nucleus or a single nucleon

1.2.1 Cross-section Calculation for Trident Production

As mentioned in the subsection above, a way of probing the physical properties of matter and the forces that govern it is through scattering experiments. These experiments require highly energetic particles, coming either from a reactor, from cosmic rays, or from a beam designed by an experiment, to either collide with one another or with a fixed target. Then, the particles resulting from this collision are analyzed and contrasted with theoretical predictions.

The scattering of particles off matter

An important concept that we are going to work with in this investigation is the *cross-section* of a certain interaction. The original concept of a cross-section comes from making the analogy of particles with hard objects with a defined size. The cross-section in this case would be the effective area around a particle inside which it is possible for a scattering to occur. For example, if we see particles as hard spheres, if we consider a target particle with radius R (left diagram on figure 1.3), a scattering event could only occur inside the area corresponding to the cross-sectional area of the target spherical particle (πR^2). Since elemental particles are not hard spheres with a defined size, and scattering occurs instead because of a the deflection of a particle off a force field (right diagram on figure 1.3), we need to make a generalization of this cross-sectional area in order to describe the likelihood of a particles interacting with another.

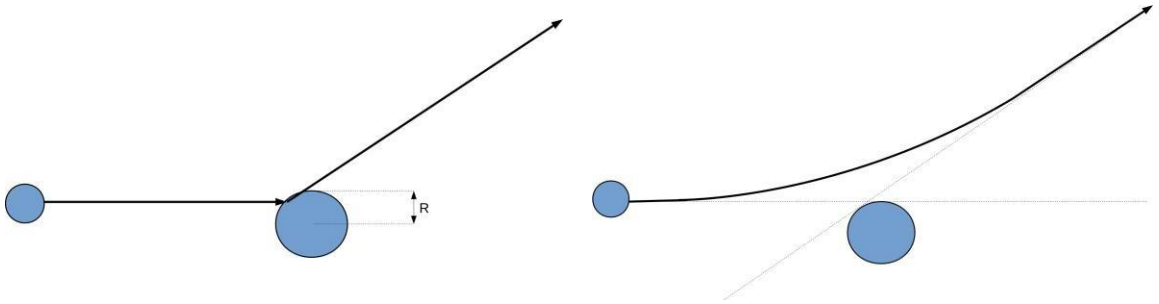

Figure 1.3: Representation of the scattering of a particle directly off a hard sphere with radius R (left), and off the force field from the target particle (right)

This generalized cross-section will not only depend on the target particle, as opposed to the case of the hard sphere, where it depended only on the radius R, but will also be dependent on the kinematic properties of the particles in the final state. Similar to the case of the cross-sectional area of a hard sphere, this cross-section will have the units of cm^2. As mentioned in the introduction, the present investigation concerns itself with the interaction of *neutrinos* with matter, specifically, trident production interactions. Therefore, one of the first steps that we need to take to study how they interact is to calculate the cross-section of this specific interaction.

The cross-section for trident production has been calculated before by other authors[7][11] in the context of a V-A theory (where $C_V = 1$ and $C_A = 1$). We first proceed with reproducing the calculations made by these authors. It is important to note, that for the this dissertation, we will use Gaussian natural units to make the calculations. Gaussian units are built by defining the electric charge in such a manner that coulomb's lawis $F = \frac{q_1 q_2}{r^2}$ Natural units work normalizing the speed of light and planck's constant to 1 ($c = 1$, $\mathsf{k} = 1$). The first step, of the calculation is to consider the three possi- ble feynman diagrams for trident production shown in figure 1.4. We can ignore the contribution of the diagram on the right, were the W boson couples directly with the photon (right diagram on figure 1.4), because the presence of two W propagator terms heavily supress its contribution.

Moreover, if we take into account the low energies at which current neutrino experiments operate2.5, as well as the how fast the form factors of nuclei decrease with q^2 (see section 1.3), we can assume safely that $q^2 << M_{W,Z}$. Therefore, we can study the weak interactions in the trident feynman diagrams as four-point effective interactions. Then, based on these two diagrams, we proceed to calculate the cross-section in the standard fashion described in particle physics textbooks, likethe one in reference [12].

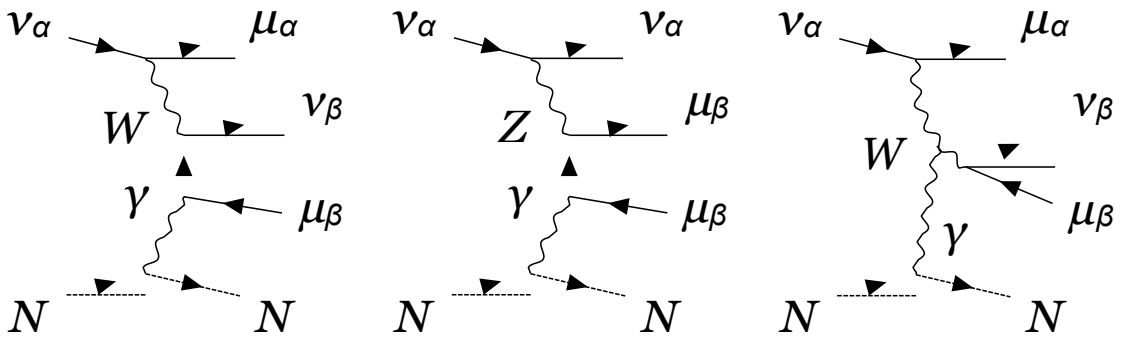

Figure 1.4: Feynman diagrams for neutrino trident production, for the general case where the dimuon pair consists of any flavour of neutrinos ($\alpha, \beta = e, \mu, \tau$). Diagrams for the charged current (CC) coupling (left), for the neutral current (NC) coupling (center), and where the W boson couples directly with the nuclear coulomb field (right). This last diagram is heavily suppressed due to the presence of two W propagators.

The golden rule for scattering

The calculation of the cross-section can be a little complicated, however there is a standard *golden rule* to calculate it. Given the scattering of two particles, like the equation below:

$$1 + 2 \rightarrow 3 + 4 + \cdots + n \tag{1.3}$$

We can get the differential cross-section for the interaction using the following golden rule:

$$d\sigma = |\mathrm{M}|^2 \frac{S}{\sqrt{(p_1 \cdot p_2)^2 - (m_1 m_2)^2}} (2\pi)^4 \delta^4(p_1 + p_2 - p_3 - p_4 \cdots - p_n) \times \prod_{j=3}^{n} \frac{d^3 p_j}{(2\pi)^3 2 p_j^0} \tag{1.4}$$

In equation 1.4 above, m_i and p_i correspond to the mass and four-momentum of the ith particle. The S term is a statistical factor that accounts for the double counting that may occur due to identical particles being in the final state, and is calculated in the following manner: For every set of identical particles in the final state, we get a factor (1/n!) where n is the number of particles in that group of identical particles. Then, all (1/n!) factors are multiplied. For example, if a final state were to have 3 particles of

type 1 and 5 particles of type 2, S would be $S = (1/3!)(1/5!)$. The information of the dynamics of the process, normally calculated using Feynman diagrams, is stored in $|M|$ which we will later calculate using the Feynman rules. Finally, the rest of the terms

in the integral represent the *phase space*, which is the integration over all the outgoing four momenta, taking into account the following restrictions:

1. Outgoing particles lie on their mass shell, that is $p^2 = m^2$. Hence the delta function $\delta(p_i^2 - m_i^2)$.
2. Outgoing particles have positive energy, which is enforced by the heaviside function $\theta(p_i^0)$
3. Energy and momentum must be conserved, which is enforced by the delta function $\delta(p_1 + p_2 - p_3 - p_4 \cdots - p_n)$.

Equation 1.4 can be simplified by performing the integrals in the p_j^0 variables, leaving us with the expression:

$$\sigma = \frac{S}{4\sqrt{(p_1 \cdot p_2)^2 - (m_1 m_2)^2}} \int |\mathrm{M}|^2 (2\pi)^4 \delta^4(p_1 + p_2 - p_3 - p_4 \cdots - p_n) \times \prod_{j=3} \frac{d^3\mathbf{p}_j}{(2\pi)^3 2\sqrt{\mathbf{p}_j^2 + m_j^2}} \tag{1.5}$$

$$d\sigma = |\mathrm{M}|^2 \frac{S}{4\sqrt{p_1 \cdot p_2)^2 - (m_1 m_2)^2}} \frac{d^3\mathbf{p}_3}{(2\pi)^3 2E^3} \frac{d^3\mathbf{p}_4}{(2\pi)^3 2E^4} \cdots \frac{d^3\mathbf{p}_n}{(2\pi)^3 2E^n} \times (2\pi)^4 \delta(p_1 + p_2 - p_3 - p_4 \cdots - p_n) \tag{1.6}$$

To begin, we start by calculating $|\mathrm{M}|^2$ by applying Feynman rules to the left and middle diagrams in figure 1.4. First, we start by labeling the momenta of the different particles in the diagram:

Incoming $\nu \rightarrow p_1$
Outgoing $\nu \rightarrow p_2$
$\mu \rightarrow p_4$
$\mu^+ \rightarrow p_3$
Intermediary $\mu \rightarrow k$
Photon $\rightarrow q$
Nucleus at start $\rightarrow P$
Nucleus at end $\rightarrow P'$

(1.7)

Then, we first calculate the M term for the NC diagram (middle diagram in figure 1.4). To do this, we start by getting the terms following the path of the $\mu^{-}(\nu_{\mu})$ backwards back to the original ν_{μ}:

$$\bar{u}(p_2)\left(\frac{-ig}{2\sqrt{2}}\gamma^{\lambda}(1-\gamma^5)\right)u(p_1) \tag{1.8}$$

Then, we add the term that corresponds to the point interaction.

$$\bar{u}(p_2)\left(\frac{-ig}{2\sqrt{2}}\gamma^{\lambda}(1-\gamma^5)\right)u(p_1)\left(\frac{ig_{\lambda\sigma}}{M_w^2}\right) \tag{1.9}$$

Where M_w is the mass of the $Z^0(W^{\pm})$ boson mediating the NC(CC) interaction. Then, we add the terms that come from following the path starting from the outgoing ν_{μ} backwards into the incoming $\mu(\nu_{\mu})$.

$$\bar{u}(p_2)\left(\frac{-ig}{2\sqrt{2}}\gamma^{\lambda}(1-\gamma^5)\right)u(p_1)\left(\frac{ig_{\lambda\alpha}}{M_w^2}\right)\times \tag{1.10}$$

$$\bar{u}(p_4)\left(\frac{-ig_w}{2\sqrt{2}}\gamma^{\sigma}(1-\gamma^5)\right)\left(\frac{i(\gamma^{\alpha}k_{\alpha}+m)}{k^2-m^2}\right)ig_e\gamma^{\mu}u(p_3)$$

If we factor the scalar terms out of the expression, reduce the ν and μ indices, and use the Dirac slashed notation so that $\gamma^{\alpha}k_{\alpha}=\not{k}$.

$$\left(\frac{-ig_w}{2\sqrt{2}}\right)\left(\frac{-ig_w}{2\sqrt{2}}\right)\left(\frac{i}{M_w^2}\right)(ig_e)\,\bar{u}(p_2)\gamma^{\lambda}(1-\gamma_5)u(p_1)\times \tag{1.11}$$
$$\bar{u}(p_4)\gamma_{\lambda}(1-\gamma^5)\frac{i(\not{k}+m)}{k^2-m^2}\gamma^{\mu}u(p_3)$$

We proceed with adding the terms for the photon propagator, as well the one for the hadronic current (current term for the nucleons/nucleus), denoted by H^{μ}. The Z term is the atomic number of the struck nucleus. Then, after contracting the indices, we get:

$$\left(\frac{-ig_w}{2\sqrt{2}}\right)\left(\frac{-ig_w}{2\sqrt{2}}\right)(ig_e)\left(\frac{i}{M_w^2}\right)\bar{u}(p_2)\gamma^{\lambda}(1-\gamma^5)u(p_1)\times \tag{1.12}$$

$$\bar{u}(p_4)\,\gamma_\lambda\,(1-\gamma^5)\,\frac{i(\not{k}+m)}{k^2-m^2}\,\gamma^\mu\,u(p_3)\,\frac{-ig_{\sigma\lambda}}{q^2}\,g_e H^\mu Z$$

Again, we factor the terms to mantain order in the calculations:

$$\left(-\frac{g_w^2}{8}\right)\left(-\frac{g_e^2 Z}{M_w^2}\right)\left(-\frac{i}{q^2}\right)\left[\bar{u}(p_2)\gamma^\lambda(1-\gamma^5)u(p_1)\right]\times$$
$$\left[\bar{u}(p_4)\gamma_\lambda(1-\gamma^5)\frac{i(\not{k}+m)}{k^2-m^2}\gamma^\mu u(p_3)\right]H_\mu \tag{1.13}$$

We then add a the $(2\pi)^4\delta^4()$ that correspond to each vertex and the $\frac{d^4q}{(2\pi)^4}$ terms that correspond to each internal momentum.

$$\left(-\frac{g_w^2}{8}\right)\left(-\frac{g_e^2 Z}{M_w^2}\right)\left(-\frac{i}{q^2}\right)\left[\bar{u}(p_2)\gamma^\lambda(1-\gamma^5)u(p_1)\right]$$
$$\left[\bar{u}(p_4)\gamma_\lambda(1-\gamma^5)\frac{i(\not{k}+m)}{k^2-m^2}\gamma^\mu(2\pi)^4\delta^4(p_2+p_4-k-p_1)(2\pi)^4\delta^4(k+p_3-q)u(p_3)\right]\times$$
$$H_\mu\frac{d^4k}{(2\pi)^4}\frac{d^4q}{(2\pi)^4}(2\pi)^4\delta^4(P_j+q-P_j) \tag{1.14}$$

We then proceed to perform the integrals on d^4k and d^4q. The integration of $\delta^4(P_j+q-P_j)$ makes sure that $q=P_j-P_j$, although we will keep using q for short hand in the calculations. Finally, according to the Feynman rules, we eliminate the $(2\pi)^4\delta^4(p_2+p_3+p_4-p_1-q)$ term, and the end result is equal to iM, therefore the amplitude that corresponds to the NC diagram (middle diagram in figure 1.4) is:

$$M_{NC}=\left(-\frac{g_w^2}{8}\right)\left(-\frac{g_e^2 Z}{M_w^2}\right)\left(-\frac{1}{q^2}\right)\left[\bar{u}(p_2)\gamma^\lambda(1-\gamma^5)u(p_1)\right]$$
$$\left[\bar{u}(p_4)\gamma_\lambda(1-\gamma^5)\frac{i(\gamma^\lambda(q_\lambda-p_{3\lambda})+m)}{(q-p_3)^2-m^2}\gamma^\mu u(p_3)\right]H_\mu \tag{1.15}$$

Now, if we repeat the calculations for the CC diagram (left diagram in figure 1.4), we get the expression:

$$M_{CC}=\left(-\frac{g_w^2}{8}\right)\left(-\frac{g_e^2 Z}{M_w^2}\right)\left(-\frac{1}{q^2}\right)\left[\bar{u}(p_4)\gamma^\lambda(1-\gamma^5)u(p_1)\right]$$
$$\left[\bar{u}(p_2)\gamma_\lambda\frac{i(\not{p}_2-\not{q}+m)}{(p_2-q)^2-m^2}\gamma^\mu(1-\gamma^5)u(p_3)\right]H_\mu \tag{1.16}$$

$$\bar{\psi}_2 \gamma^\mu \psi_1 \bar{\psi}_4 \gamma_\mu \psi_3$$

Now we are able to apply a Fierz Transformation in order to give the equation above the same structure as the expresion for the NC current in equation 1.17:

$$\mathrm{M}_{CC} = \left(\frac{g_w^2}{8}\right)\left(\frac{g_e^2 Z}{M_w^2}\right)\left(\frac{1}{q^2}\right)\left[\bar{u}(p_2)\gamma^\lambda(1-\gamma^5)u(p_1)\right] \left[\bar{u}(p_4)\left(-\gamma_\lambda\frac{i(\not{p}_4 - \not{q} + m)}{(p_4 - q)^2 - m^2}\gamma^\mu(1-\gamma^5)\right)u(p_3)\right] H_\mu \tag{1.17}$$

Finally, by adding for contributions, we get the expresion for the total M:

$$\mathrm{M} = \mathrm{M}_{CC} + \mathrm{M}_{NC} = \left(\frac{g_w^2}{8}\right)\left(\frac{g_e^2 Z}{M_w^2}\right)\left(\frac{1}{q^2}\right)\left[\bar{u}(p_2)\gamma^\lambda(1-\gamma^5)u(p_1)\right] \left[\bar{u}(p_4)\left(\gamma_\lambda(1-\gamma^5)\frac{i(\not{q} - \not{p}_3 + m)}{(q-p_3)^2 - m^2}\gamma^\mu + \gamma^\mu\frac{i(\not{p}_4 - \not{q} + m)}{(p_4 - q)^2 - m^2}\gamma_\lambda(1-\gamma^5)\right)u(p_3)\right] H_\mu \tag{1.18}$$

By identifying the leptonic current in equation 1.18 and labeling it L^μ, as well as making the replacements $g = \sqrt{4\pi\alpha}$ and $G = \frac{g_w}{\sqrt{2}}\frac{1}{8 M_w^2}$, we have:

$$\mathrm{M} = \left(\frac{g_w^2}{8(M_w)^2}\right)\left(\frac{g_e}{q^2}\right) L^\mu H_\mu$$

$$\mathrm{M} = \frac{G}{\sqrt{2}}\left(\frac{4\pi\alpha Z}{q^2}\right) L^\mu H_\mu \tag{1.19}$$

$$|\mathrm{M}|^2 = \frac{G^2}{2}\left(\frac{4\pi\alpha Z}{q^2}\right)^2 L^\mu H_\mu L^\nu H_\nu \tag{1.20}$$

$$|\mathrm{M}|^2 = \frac{G^2}{2}\left(\frac{4\pi\alpha Z}{q^2}\right)^2 L^{\mu\nu} H_{\mu\nu}$$

Where we make the following definitions:

$$L^{\mu\nu} = L^{\mu} L^{\nu}$$
$$H_{\mu\nu} = H_{\mu} H_{\nu} \tag{1.21}$$

Now we are ready to apply the golden rule described in equation 1.6. In that equation we replace particles 1 and 2 with the incoming ν and initial nucleus, with corresponding four momentums $p_1 = (E_1, \mathbf{p}_1^1, \mathbf{p}_1^2, \mathbf{p}_1^3)$ and $p_2 = (M, 0, 0, 0)$, assuming the nucleus to have a mass M and to be at rest in the lab frame of reference, as well as the incoming neutrino to be massless, resulting in $E^2 = (\mathbf{p}^i_1)^2$. The rest of the

particles, as well as their corresponding energies and momentums are labeled following the convention set in the set of equations 1.7.

$$\sigma = \frac{G^2(4\pi)^2\alpha^2Z^2}{2}\frac{1}{q^4}\frac{1}{4\sqrt{(ME)^2}}\int \frac{d^3\mathbf{p}_2}{(2\pi)^3 2E_2}\frac{d^3\mathbf{p}_3}{(2\pi)^3 2E_3}\frac{d^3\mathbf{p}_4}{(2\pi)^3 2E_4}\frac{d^3\mathbf{P}_j}{(2\pi)^3 2E_j}\times$$
$$(2\pi)^4\delta(p_1+q-p_2-p_3-p_4)L^{\mu\nu}H_{\mu\nu}$$
$$= \frac{2Z^2\alpha^2G^2}{(2\pi)^6}\int \frac{d^3\mathbf{P}_j}{2E_j}\frac{d^3\mathbf{p}_2}{2E_2}\frac{d^3\mathbf{p}_3}{2E_3}\frac{d^3\mathbf{p}_4}{2E_4}\times\delta(p_1+q-p_2-p_3-p_4)\frac{1}{4ME}L^{\mu\nu}\frac{1}{q^4}H_{\mu\nu} \quad (1.22)$$

Using Casimir's trick, which is also explained in most introductory particle physics textbooks, like reference [12], we can reduce $L^{\mu\nu}$ to a product of traces. For the trace reductions, as well asother cumbersome calculations with indices, we have made use of the FeynCalc package for Wolfram Mathematica[13]:

$$L^{\mu\nu} = \mathrm{Tr}\left[\gamma^\sigma(1-\gamma^5)(\not{p}_1+m)\gamma^\nu(1-\gamma^5)(\not{p}_3+m)\right]\times$$
$$\mathrm{Tr}\left[\gamma^\mu\frac{1}{-\not{p}_4-\not{q}+m}\gamma^\rho(1-\gamma^5)+\gamma^\sigma(1-\gamma^5)\frac{1}{\not{q}-\not{p}_3+m}\gamma^\mu\times\right.$$
$$\left.(-m-\not{p}_2)\gamma^\nu\frac{1}{\not{q}-\not{p}_3+m}\gamma^\lambda(1-\gamma^5)+\gamma^\lambda(1-\gamma^5)\frac{1}{-\not{p}_4-\not{q}+m}\gamma^\nu(m-\not{p}_4)\right] \quad (1.23)$$

It is important to note that, since the vector and axial-vector couplings C_V and C_A remain the same, the total cros-ssection for the neutrino and antineutrino trident cross-sections are the same $\sigma_\nu^{\text{trident}} = \sigma_{\bar{\nu}}^{\text{trident}}$.

Now that we have successfully calculated the matrix element of the leptonic current $L_{\mu\nu}$, we note that the matrix element representing the hadronic current $H_{\mu\nu}$ depends on the spin of the target. For *coherent* processes, where we assume the nucleus as a spin-0 target, we have the interaction:

$$\nu_\mu + N \rightarrow N + \mu^+ + \mu^- + \nu_\mu \quad (1.24)$$

Where the hadronic current adopts the form [11]

$$H_{\mu\nu}(P, q) = H_{\nu\mu}(P, q) \quad \frac{1}{} \Sigma - \frac{1}{} \Sigma$$

$$= 4|F(q^2)|^2 \quad P_\mu - {}_2 q_\mu \quad P_\nu - {}_2 q_\nu \tag{1.25}$$

As noted by [7], due to the current conservation at the vertices of the photon propagator:

$$q_\mu L_{\mu\nu} = q_\nu L_{\mu\nu} = q_\mu H_{\mu\nu} = q_\nu H_{\mu\nu} = 0 \tag{1.26}$$

The effective part of $H_{\mu\nu}$ can be written for interactions with a spin-0 nucleus as:

$$H_{\mu\nu} = 4P_\mu P_\nu F^2(q^2) \tag{1.27}$$

The nuclear formfactors $F(q^2)$, restrict the high-energy contribution of the coherent crosss-section, since they fall quickly as q^2 increases. This makes it interesting to also tudy the *incoherent* scenario, where the neutrino scatters off individual nucleons, and therefore is linked to the nucleon form factor and not the nuclear one and thus falls off at a slower rate.

$$\nu_\mu + p/n \rightarrow p/n + \mu^+ + \mu^- + \nu_\mu \tag{1.28}$$

The hadronic current part for the incoherent scattering off a spin-$\frac{1}{2}$ nucleon can be written as [11]:

$$H_{\mu\nu}(P,q) = 4P_\mu P_\nu (G_E^2 + xG_M^2)/(1+x) + \delta_{\mu\nu} q^2 G_M^2 \tag{1.29}$$

Where:

$$x = \frac{q^2}{4M^2}$$

$$G_M = F_1 + F_2$$

$$G_E = F_1 - xF_2$$

From these expressions it becomes evident that, in order to calculate the contraction $H^{\mu\nu} L_{\mu\nu}$, we only require to be able to calculate $P_\mu L_{\mu\nu} P_\nu$ and $\delta_{\mu\nu} L_{\mu\nu}$. We checked that we could reproduce exactly these two expressions in the context of V-A ($C_A = C_V = 1$) theory, which has already been calculated by reference [7] and shown in the appendix A of their paper. In order to translate these calculations to the SM, we add the axial and vector coupling in the equation 1.18, which gives:

$$M = \frac{g_w^2}{8(M_W c)^2} \frac{g_e^2 Z}{q^2} \bar{u}(p_2)\gamma^\mu (C_V - C_A\gamma^5) u(p_1) \; i(\gamma^\mu (q_\mu - p_{3\mu}) + mc) \; \bar{u}(p_4) \; \gamma_\mu (C_V - C_A\gamma^5) \; (q - p) \; \gamma^\lambda \frac{i(\gamma^\mu (p_{4\mu} - q_\mu) + mc)}{} \gamma \; (C - C\gamma) \; u(p) H \tag{1.30}$$

$$(p_4 - q)^2 - m^2c^2 \quad {}^{\mu} \quad {}^{V} \quad {}^{A} \quad {}^{5} \quad {}^{3} \quad {}^{\lambda}$$

We then follow the same procedure to calculate the corresponding $P_\mu L_{\mu\nu} P_\nu$ and $\delta_{\mu\nu} L_{\mu\nu}$ constractions, this time the use of FeynCalc is obligatory, since the number of

terms that appear is unmanageable without a computer. The expressions for $P_\mu L_{\mu\nu} P_\nu$ and $\delta_{\mu\nu} L_{\mu\nu}$, equivalent to the ones on the appendix A of reference[7], are shown in Appendix A of this paper.

As it can be seen from expression 1.27, the form factors ($F(q^2)$) factor out of the currenttermsforthecoherentprocess, andasa resultscalethe differentialcross-section directly. Because of their significant effect on the cross-section, we saw convenient to study the effect that the use of different models for charge distributions had on the nuclear form factors.

1.3 Study of the Nuclear Form Factors

One big advantage of equation 1.27, is that the form factor (FF) is factorized outside the equation, making the exchange between the FF for **nuclei**, for the coherent case, and **nucleons** for the incoherent case straightforward.

In the same way as reference[7], we have considered the *exponential*, *dipole* form factors, defined as follows:

The **exponencial** parametrization models the nuclear form factor with the following equation:

$$F(q^2) = e^{q^2 R_0^2 / 10} \tag{1.31}$$

The **dipole** parametrization models the nuclear form factor with the followinf equation.

$$F(q^2) = \frac{1}{(1 - q^2 R_0^2/20)^2} \tag{1.32}$$

Another way to parametrize the nuclear FF is tocalculate it as the Fouriertransform of the nuclear charge density $\rho(r)$[14]. We considered two models for the nuclear charge distribution, which could then be used tocalculate more precise form factors by taking the fourier transform in the following manner:

$$F(q^2) = \frac{\int \rho(\mathbf{r}) e^{iq\cdot\mathbf{r}} d^3\mathbf{r}}{\int \rho(\mathbf{r}) d^3\mathbf{r}} \tag{1.33}$$

The models we took into consideration were the Fermi Distribution, and the Harmonic Oscillator distributions for the nuclear charge density.

The **Fermi distribution** parametrization models the nuclear form factor with the following equation

$$\rho(r) = \frac{\rho_0}{1 + e^{(r-c)/z}} \tag{1.34}$$

As it can be noticed from the equation, this distribution is a two-parameter parametrization that depends on the parameters c and z. The parameters used for the different atoms were taken from [15].

The **harmonic oscillator** parametrization has only one free parameter (a), which was obtained as well from reference [15]. This charge density model is described with the following equation:

$$\begin{aligned}
\rho(r) &= \rho_0(1 + \alpha(r/a)^2)exp(-(r/a)^2) \\
\alpha &= \alpha_0 a_0^2/(a^2 + \frac{3}{2}a_0^2 - a^2)) \\
a_0^2 &= (a^2 - a_p^2)A/(A-1) \\
\alpha_0 &= (Z-2)/3 \\
a_p^2 &= (r^2)_{proton}
\end{aligned} \tag{1.35}$$

Figure 1.5 shows how the three different parametrizations agree with experimental data [16]. The first thing that can be noticed from these figures is that the fermi distribution parametrization agrees much more closely to the data than the dipole or the exponential parametrizations. This was also noted by reference [7] and was the reason why they chose the two-parameter fermi distribution for the simulations in their final results. Although the plot on oxygen also shows that the harmonic oscillator parametrization agrees very well with data for oxygen, reference [15] does not contain the necessary a parameter for all the nuclei that were relevant for our investigation. Therefore, we chose to use the Fermi distribution, both for its agreement with data, as well as the availability of the parameters for various nuclei. The second thing that can be noted from the plots below, is how quickly the form factor value falls with an increase in the modulus of q. This limits the relevance of events in the vicinity of $|q| = 0.4GeV$ for argon and $|q| = 0.3GeV$ for oxygen.

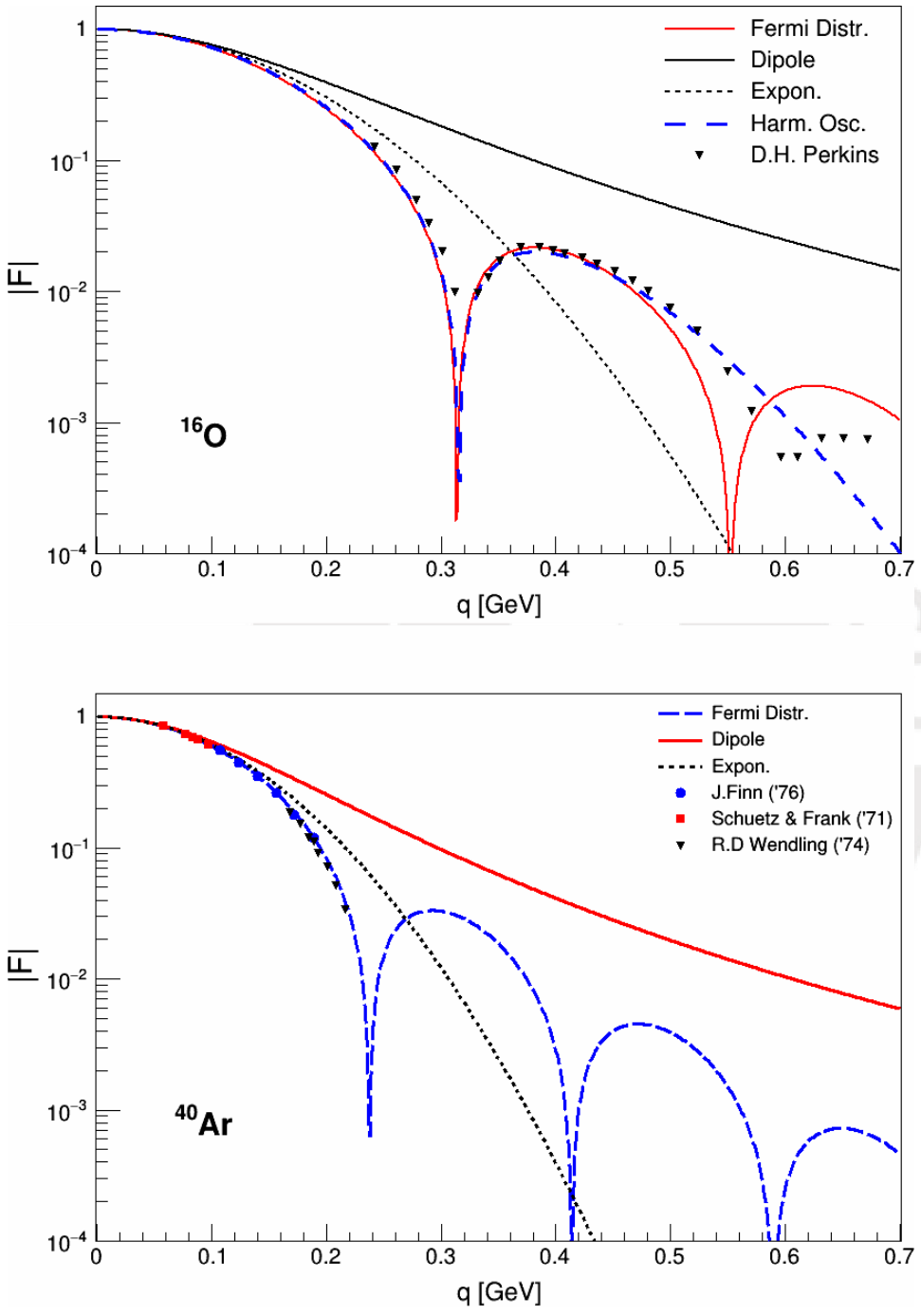

Figure 1.5: Form Factor models for Oxygen (left) and for Argon (right)

1.4 Backgrounds for Trident Production

1.4.1 Charm Production

Charm production interactions are those in which a charmed meson/baryon is produced. The short lifetime of charmed baryons, like the λ_c^+, for example, which has a lifetime of $2.00 \pm 0.06 \times 10^{-13} s$ makes it impossible for current neutrino detectors to resolve the resulting μ^+ as not coming from the interaction vertex.

$$\nu_\mu + s/d \rightarrow \mu^{\mp} + c \qquad (1.36)$$
$$c \rightarrow s/d + \mu^{\pm} + \nu_\mu$$

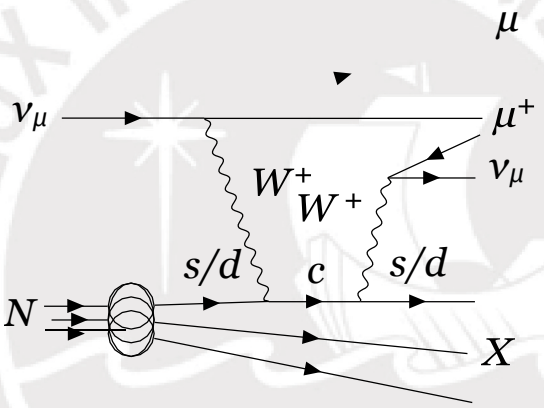

Figure 1.6: Charm production diagram.

There is a wide variety of charmed baryons/mesons that can be produced in a charm production interaction, however, early in the investiagation we noticed that if we applied the following cuts (which stem from the discussion in section 2.2) to the charm production signal:

1. There are no more than two μ's, which should be oppositely charged, in the final state

2. There are no more thatn 4 particles in the final state (ν, μ^-, μ^+, and an outcoming nucleon)

Then, the μ^+, would come solely from the decay of λ_c^+'s, produced in a Quasi-elastic (QEL) CC interaction. This fact is very important, because it means that being able to detect low energy showers coming from the main interaction vertex reduces the most

important backgrounds from charm production. This is evidenced by the fact that in reference [6] about charm production in the Tevatron λ_c^+ decays are of the least important contributions to the signal, mostly because low capacity of the detector to detect low energy showers.

Another important detail about charm production of $\lambda_c^{+\prime}$s , is that current conservation in this CC interaction results in neutrons being the only possible nucleons for the final state. Therefore, the background signal does not increase if we change from studying coherent interactions to incoherent ones.

1.4.2 Pion Production

Inclusive single π^+ production is the name given to the group of processes that generate a single π^+ in the final state. The feynman diagram showing an example of one of such processes is shown in figure 1.7. When considering the $\pi^{+\prime}$s produced inside of the detector, we identified two possible types of background processes: **contained pions** and **passed pions**.

$$\begin{aligned} \nu_\mu + N \rightarrow \mu^{\mp} + X + \pi^{\pm} \\ \pi^{\pm} \rightarrow \mu^{\pm} + \nu_\mu \end{aligned} \tag{1.37}$$

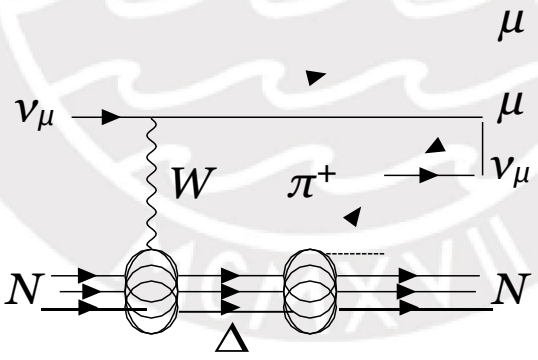

Figure 1.7: Pion production diagram.

Contained Pions These are single pion production events where the track left by a μ^+ and the track, left by the π^+ it decayed from, form an angle that is smaller than the detector's angular resolution. This would result in both tracks to be potentially misreconstructed as a single track of a μ^+ coming from the main vertex. This track,

when joined with the μ^- track from the original CC interaction, would result in a dimuon signal, similar to that of trident production. It is important to note that, since the lifetime of the π^+ is sufficiently big of the detector to detect a displaced vertex, this background is given a different treatment as the charm production background, where λ_c^+'s lifetime is small enough for it to not be detected before decaying. Therefore we deemed necessary the analysis of the angle between π^+ and μ^+ tracks for the selection of this type of background.

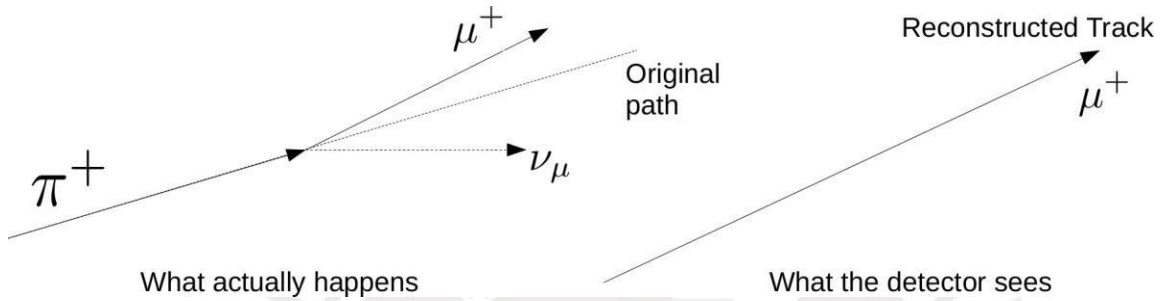

Figure 1.8: Diagram describing how the track of a π^+ that decays into a μ^+ may be misreconstructed as a μ^+ track coming from the interaction vertex

Passed Pions For the purpose of this investigation, we will refer to the pions that go through the detector without interacting as passed pions. This is a very rare occurence, since most experiments usually haveastrategy tocontain the hadronic showers produced inside of the fiducial region. However, since the cross-section of trident production is very small, such occurrences may be a relevant background for trident production.

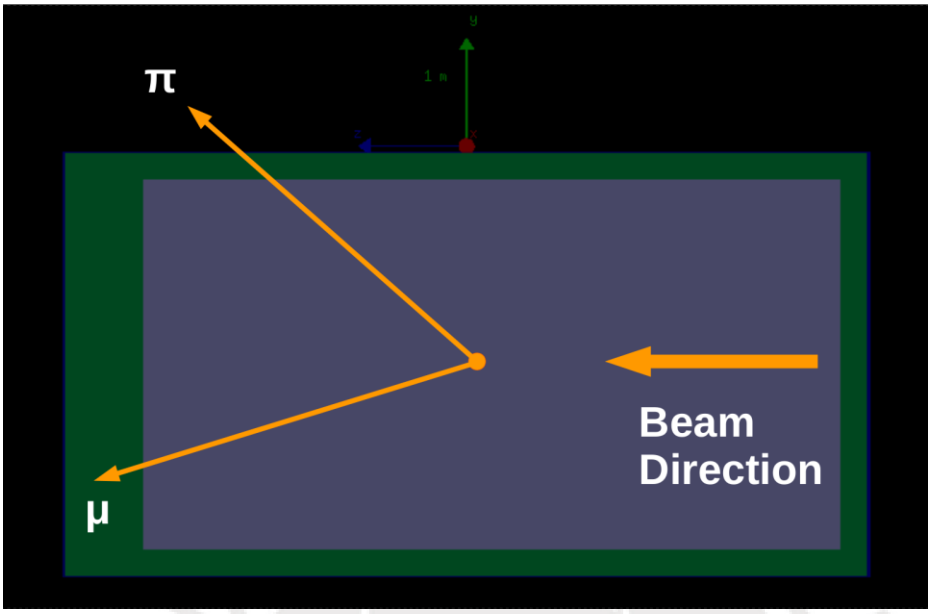

Figure 1.9: Passed pions diagram in the context of a DUNE-like detector.

1.5 Proton Distributions

It is important to note that, in the case of incoherent trident generation, when the neutrino interacts with a proton, this proton is expected to come out of the main interaction vertex, similar to a quasi-elastic interaction (QEL). For the purpose of this dissertation, we did not use the kinetic properties of this proton as a criteria to discriminate trident from background events. Nonetheless, as it is shown on figure 1.10, it could be possible to eliminate a large portion of background events by making a cut at 0.1 GeV in the proton kinetic energy.

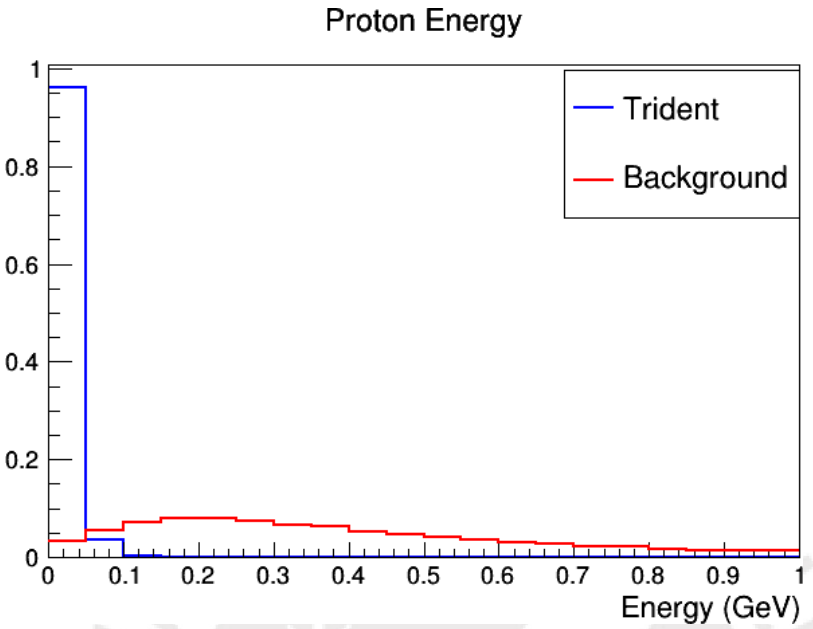

Figure 1.10: Normalized distributions of the energies of the protons coming from the main vertex for the trident (blue) and background (red) signals.

Chapter 2

Experimental Observables and analysis Methods

2.1 Experimental Observables

As described in the previous section, trident production is expected to generate a μ^+ μ^- pair. We considered a set of observables a detector might be able to measure, that would help us distinguish the trident signal from the background. We chose the six variables described in Table 2.1. They are also described graphically in figure 2.1. The first variable is the Z-position of the main interaction vertex. This variable was chosen, at first, because for the backgrounds that come from π^+ decay. The position in the detector at which they are produced is important, because the π^+ that are produced upstream in the detector will have more time to decay than the ones that have their main vertex further downstream. Second, for the case of **passed pions**, since the closer to the edges of the detector the π^+'s are generated, the more likely they are to become a passed pion background, since they need to go through less material in order to escape the detector. This can be seen very clearly in figure 2.2, where the graph for the background Z_{int} falls off dramatically as one progresses along the Z-axis. Variables 2 and 3 are the angles that the positive and negative μs, respectively, form with the Z axis.

These variables were chosen because, according to the kinematic distributions calculated by reference [7], both the μ^+ and th μ^- are expected to form small angles with the z axis for trident production. For the background interactions, however, we expect to have larger angles for the μ^+'s, mostly because they originate from the decays of particles, and it relies on the particles being of high enough energy to carry enough momentum to be likely to form a small angle with the Z axis. Variable 4 is the angle between the positive and negative tracks detected. It should be strongly correlated

Observable	Description	Reconstruction Requirements
Z_{int}	Longitudinal position of interaction vertex	Vertexing
θ_+	Track polar angle of positive particle (w.r.t. beam axis)	Tracking, charge ID
θ_-	Track polar angle of negative particle (w.r.t. beam axis)	Tracking, charge ID
θ_{+-}	Angular separation between positive and negative particle tracks	Tracking
E_{+-}	Energy difference between positive and negative particles	Muon calorimetry (charge ID for sign)
W_{+-}	Invariant mass of positive and negative particles	Full muon momentum

Table 2.1: Variables taken into account for analysis

with variables 2 and 3, but may still offer new information, since the tracks are in a 3D space. Finally, variables 5 and 6 are the energy difference and the invariant mass of the dimuons. These variables will then be used as the features on which the algorithms, described in section 2.5, will be trained.

Taking into account that, depending on detector design, all six variables described on Table 2.1 will not always be available for analysis, we defined 4 different scenarios, described on Table 2.2, of sets of variables that represent the limitations of different detector designs. Scenario 1 describes a detector that has the capacity of determining the charge of a particle, as well as is energy and momentum, and thus is also able to calculate the invariant mass. Scenario 2 describes a detector that is limited in that it cannot distinguish the charge of the particle pair that comes out of the main vertex, possibly because it does not have a magnetic field for charge and momentum detection. However it may still be possible for this detector to measure a particle's momentum and energy by means of dE/dX analysis. Both of these scenarios describe situations in which we assume that the detector has a perfect way to contain all pions that are produced inside of it. Therefore, in the TMVA analysis, we won't be considering the **passed pions** background when running the analysis for scenarios 1 and 2.

Now, scenarios 3 and 4 do concern themselves with the realistic scenario in which a detector may have π^+ that manage to escape its calorimetry and therefore, when running the TMVA analysis in that set of variables, we do include the passed pions in the background signal. Scenario 3, similar to scenario 1, describes a detector that

Scenario	Availableobservables					# of vars
1		θ_+	θ_-	θ_{+-}	E_{+-}	W_{+-}	5
2				θ_{+-}	$\lvert E_{+-}\rvert$	W_{+-}	3
3	Z_{int}	θ_+	θ_-	θ_{+-}	E_{+-}	W_{+-}	6
4	Z_{int}			θ_{+-}	$\lvert E_{+-}\rvert$	W_{+-}	4

Table 2.2: Studied scenarios of availability of observables

posseses a magentic field, and therefore is able to distinguish which track corresponds to the positively charged particle, and which track corresponds to the negatively charged one. Finally, scenario 4, similar to scenario 2, describes a detector that does not posess a magnetic field, but does have otherwise a way to measure the particle's energy and momentum.

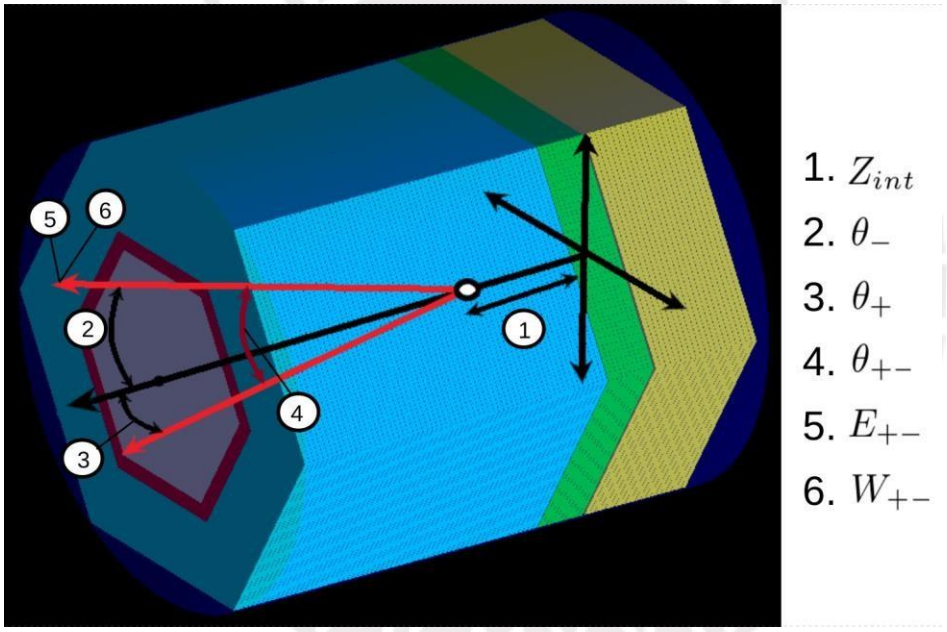

Figure 2.1: Kinematic distributions for the 6 variables selected, for signal and background

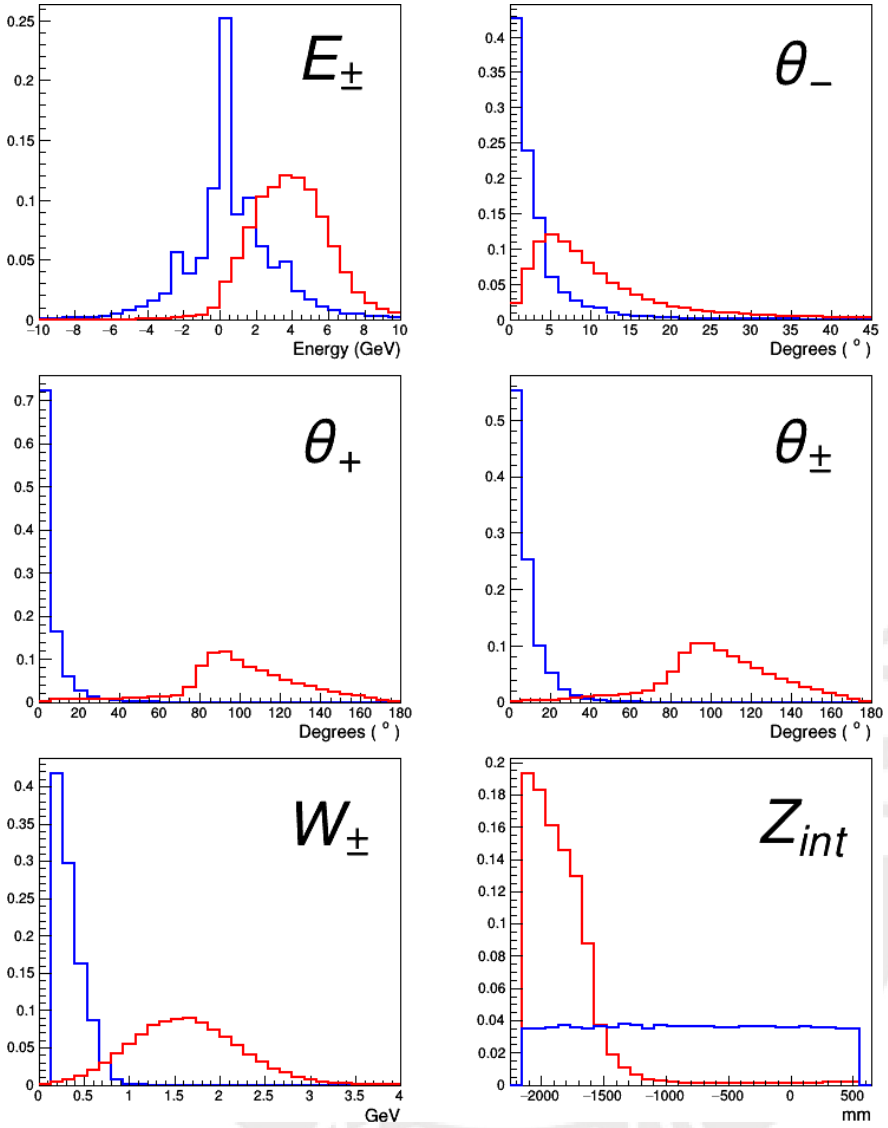

Figure 2.2: Signal (Blue) vs. Background (Red) distributions of input variables for a MINERνA-lis detector.

2.2 Selection Criteria

Trident production produces a very distinct dimuon signal, however there some characteristics of the signal that we should also take into account.

For **coherent** Trident production:

1. Final state must contain only two oppositely charged μ's

2. The final state must contain only the μ's and the recoiling nucleus (the neutrino is not mentioned since it won't be detected)

For **incoherent** Trident production:

1. Final state must contain only two oppositely charged μ's
2. The final state must contain only the μ's, a single free nucleon, and the target nucleus (the neutrino is note mentioned since it won't be detected)

As you can see, the lack of hadronic showers is a characteristic of both the coherent and incoherent trident signal. This allows us to limit their possible backgrounds a lot. However, it is not a trivial task to detect neutrons in modern neutrino experiments, as described for the case of charm production in the previous chapter, thus we have chosen to take into account all events that produce neutrons for the coherent signal, since assuming that they are never identified would give us a conservative estimate of the backgrolund. Furthermore, as evidenced by the description above, for the incoherent case it is still possible to accept events that produce a proton in the final state.

2.2.1 Cuts used to select Background candidates

Now, if we analyze the three possible sources of background described in section 1.4, which we already know are capable of producing a $\mu^+\mu^-$ pair, we need to decide which cuts are the minimum necessary in order for them to be confused for the trident signal.

- For coherent interactions
  - For Charm production: Final state particles consists of a $\mu^+\,\mu^-$ pair as well as a ν (not visible) and a neutron.
  - For Pion production: Final state particles consists of a μ^-, a π^+ as well as a ν (not visible) and a neutron (or none, in the case of coherent pion production).
  - For the *contained pions* case of single pion production, we also require that the angle between the tracks of the μ^+ and its parent π^+ is smaller than the detector's angular resolution.
- For incoherent interactions (all backgrounds): Final state particles consists of a $\mu^+\,\mu^-$ pair as well as a ν (not visible) and a nucleon (proton or neutron). All other cuts are identical to the coherent case.

  Note: As discussed in section 1.4.1, only neutrons are possible in the final state, and thus the charm production background does not change between the coherent and incoherent case.

2.3 Trident Production Simulation

Asmentioned in the introduction, the trident signal eventswere generated bymeans of implementing the interaction in the GENIEmontecarlo generator. Thecross-section implemented was the one calculated in 1, iwth the C_V and C_A coefficients set to 1. Then in order to account of the interference of the Z and $W^{\pm}$ bosons, we multiplied the cross section by a factor $\sqrt{C_V^2 + C_A^2}$ [4]. Appart of the hardships that comes with making additions a complex simulation framework such as GENIE, we faced the problem of sampling the available phase space for trident production. The problem arises from the fact that the trident production cross section is very peaked, and as a result, a uniform sampling of the phase space becomes very inefficient. Originally, when the cross section was calculated by W.Czyz, G.C. Sheppey and J.D. Walecka (CSW)[11], it was described in terms fo six variables $x1 \ldots x6$. Then, in order to make the calculations faster, Lovseth *et al*.[7], made a convenient transformation into a new set of variables $u1 \ldots u6$, in order to be able to sample the distribution in a version of the phase space in which it is not as peaked.

At the present stage of our implementation of trident production in GENIE, these Lovseth transformations have been implemented for the generation of events for the coherent case. For the incoherent case, the generation is still made by sampling the original phase space defined by the variables $x1 \ldots x6$ defined by [11]. In this phase space, wewere forced togenerate amuchlarger sample, compared tothecoherent case, since we needed to make sure the phase space was being sampled correctly. Future plans include the implementation of a Vegas-like algorithm, that could make an adaptive sampling of the phase space, thereby making the sampling more efficient, even when doing it uniformly. For now, however, our GENIE implementation can only generate weighted events. Thankfully, the ROOT TMVAtoolkit is well suited to analyze signals of weighted events.

One crosscheck we made to makesure that our implementation of the trident generator in GENIE was working correctly, was to generate cross section splines by making GENIE inegrate internally the differential cross section that we implemented in it. For this the VEGAS algorithm from the GSL library was used. This algorithm uses an adaptive sampling of the phase space, that makes the integration very fast, even with a peaked cross section like that of trident for the incoherent case. Figure 2.3 shows the comparison of the GENIE integrated cross section for the fermi form factor with the calculations made by Lovseth. The calculations made by CSW for the exponential and dipole form factor are algo compared with the calculations using an integration script made in Mathematica, since those form factor have not yet been added to the GENIE implementation. Finally, the GENIE calculations for the incoherent case are

also compared woththe calculations by Lovseth, as well as the ones made by the paper by R.W. Brown *et al.*[17].

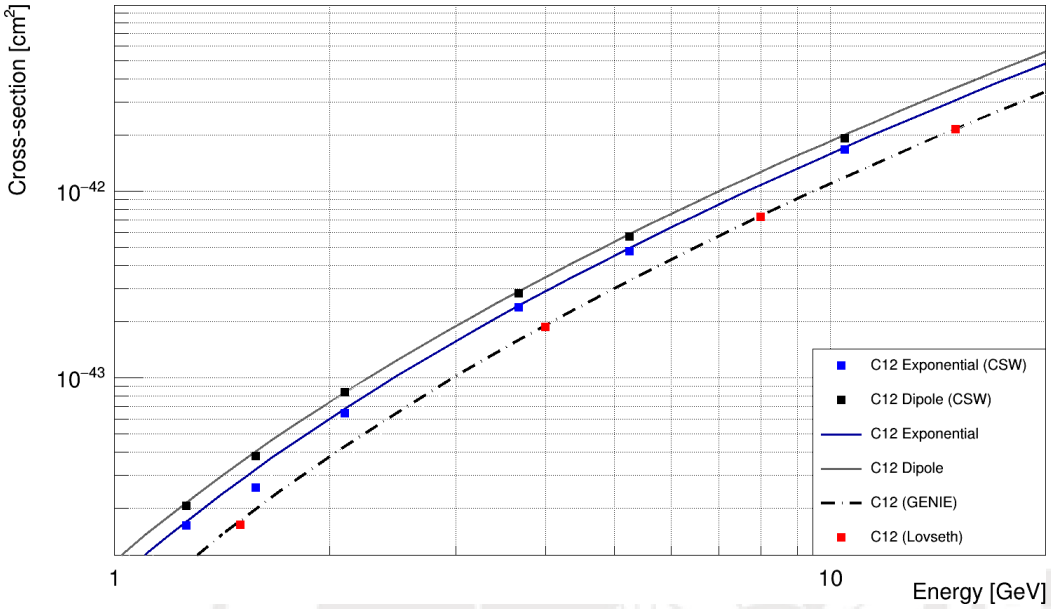

Figure 2.3: Comparison of the Coherent cross-sections of the CSW[11] paper with the cross-sections integrated in Mathematica for the exponential and dipole form factors. The Lovseth[7] cross section, calculated with the Fermi form factor, is compared with the cross section implemented in GENIE.

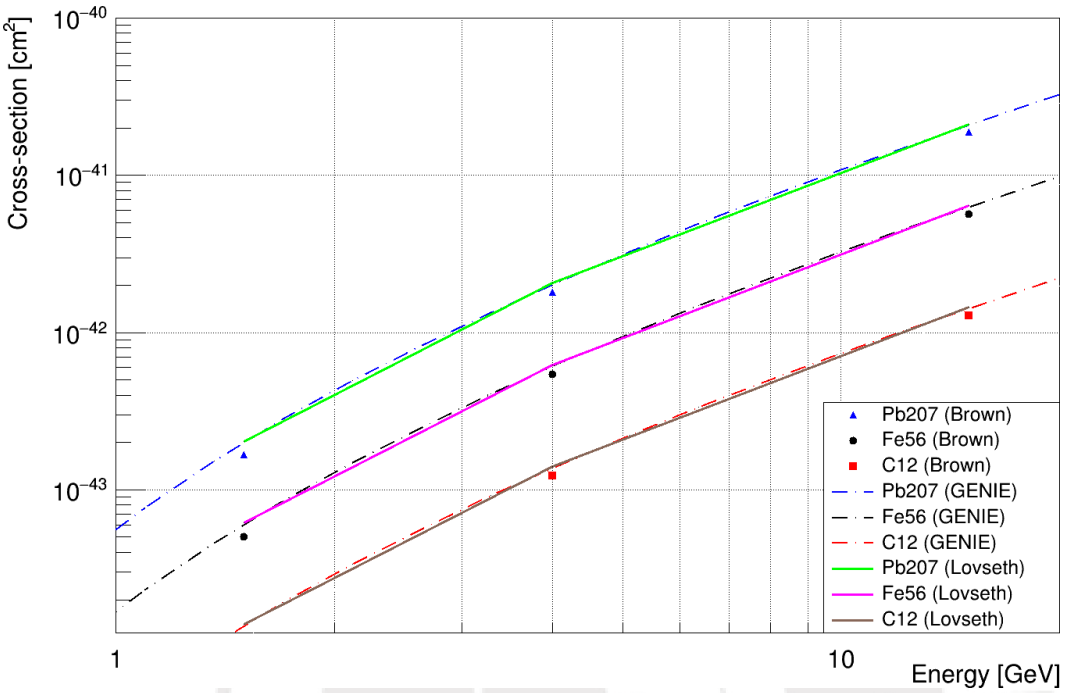

Figure 2.4: Comparison of the nuclear Incoherent cross-sections in the Lovseth[7] and Brown[17] references with the cross-section integrated in our GENIEimplementation

2.4 Experimental Configuration and Background Simulation

The background interactions were simulated in using the GENIE montecarlo simulator in a similar manner to the trident signal. Also, because π^+ backgrounds (contained pions, passed pions) depend on the way π^+'s interact with the detector, we also saw fit to use the GEANT4 simulation toolkit[18] to propagate the particles generated in GENIE inside of simplified detector geometries, representing the designs for the MINERνA detector, as well as the DUNE Near Detector (ND) straw tube tracker (STT) and liquid argon time projection chamber (LArTPC) proposals[19].

2.4.1 GENIE Simulation

At first, the GENIE v2.12.4 montecarlo generator was used to generate an inclusive sample of events. As explained in a previous section, the background signals depend

on the decay of $\pi^{+\prime}$s inside of the detector. For all the events produced, which qualified as candidates for background events, the kinematic information of the pions generated was used as input for the Geant4 simulation.

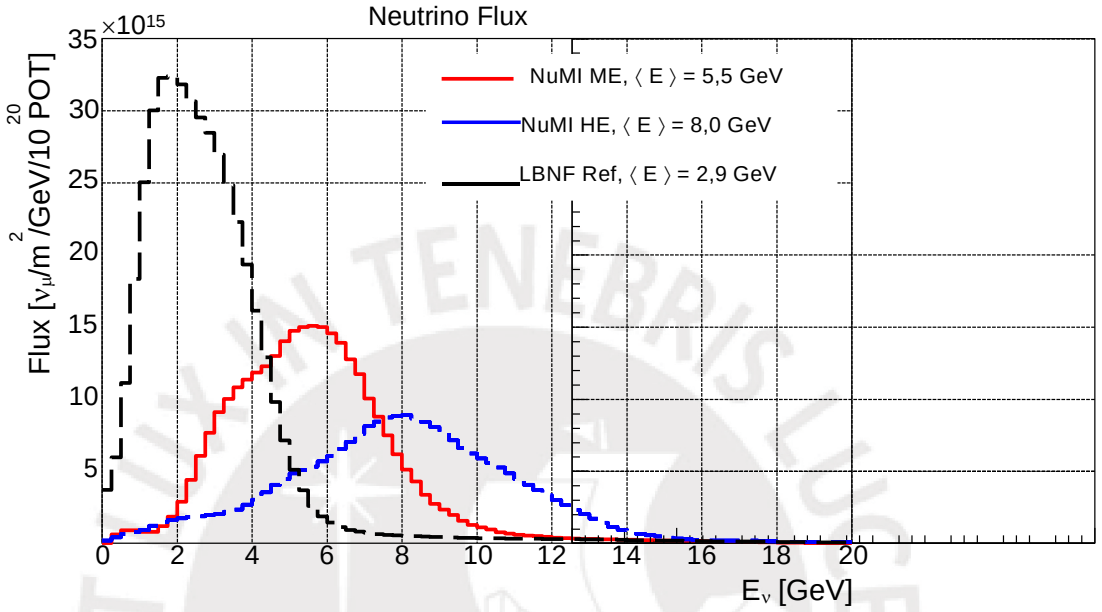

Figure 2.5: Beam configurations used for the background simulation.[20][21]

2.4.2 Particle Propagation in Geant4

Then, in order to simulate the background signals coming from π^+ decay, particles were propagated in geometries emulating the MINERνA Detector, as well as the DUNE ND using Geant4 v10.3.1.

- A MINERνA-like Detector, shaped like an hexagonal prism.
- A plastic scintillator approximation of the DUNE Near-Detector, consisting of a cubic plastic scintillator region, surrounded y electromagnetic calorimeter regions, as specified in plastic scintillator design for the DUNE ND, proposed on the March DUNE Collaboration ND Workshop [22].
- A liquid argon approximation of the DUNE Near-Detector, as specified in the liquid argon design for the DUNE ND, as proposed in the same DUNE Collaboration ND Workshop[23].

For the DUNE STT ND and MINERνA detectors, we generated the GENIE samples using the same proportions of carbon and hydrogen reported by the detector designs for their tracker regions. For the DUNE ND argon design, events were generated only on argon. For the MINERνA-like detector, we used two different fluxes for simulation, the Medium energy (ME) flux, and the High energy (HE) flux[24], while for the DUNE ND detectors, we used the LBNE's flux[21].

2.4.2.1 MINERνA-like Detector

The geometry portrayed in Figure 2.6 is the MINERνA-like volume that was used for the background simulations. The fiducial volume has the shape of a hexagonal prism, with a 465mm apothem. The fiducial volume is in turn surounded by electromagnetic and hadronic calorimeter rings, which are designed according to the same specifications used for the MINERνA Detector[25]. There is also an electromagnetic calorimeter region, as well as a hadronic calorimeter region downstream from the tracker, which are also also designed based on the same bibliography.

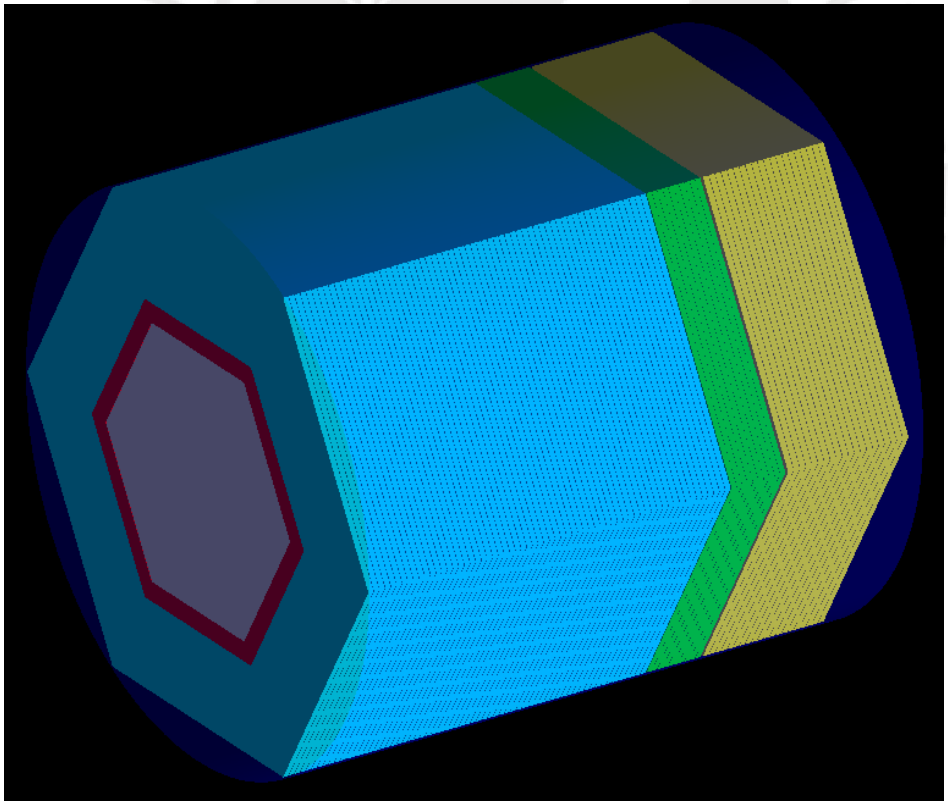

Figure 2.6: Geometry used for the simulation of the MINERνA-like detector

2.4.2.2 DUNE ND - Straw Tube Tracker Proposal

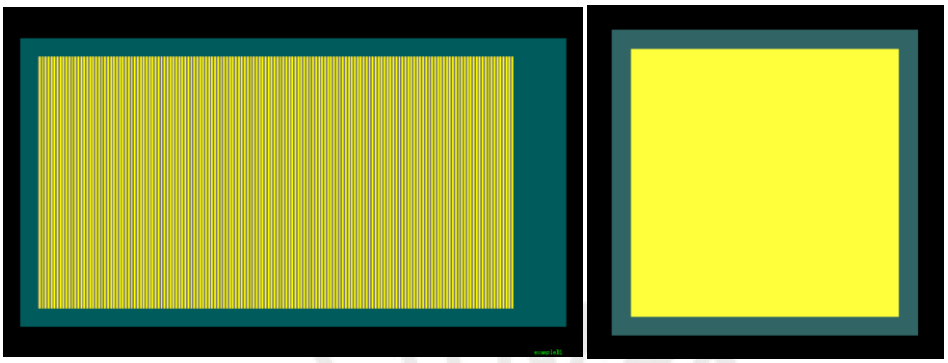

Figure 2.7: Cross section (left) and front view of fiducial region and electromagnetic calorimeter for the STT proposal. STT planes in the fiducial region are shown in yellow and the electromagnetic calorimeter surrounding them is shown in green.

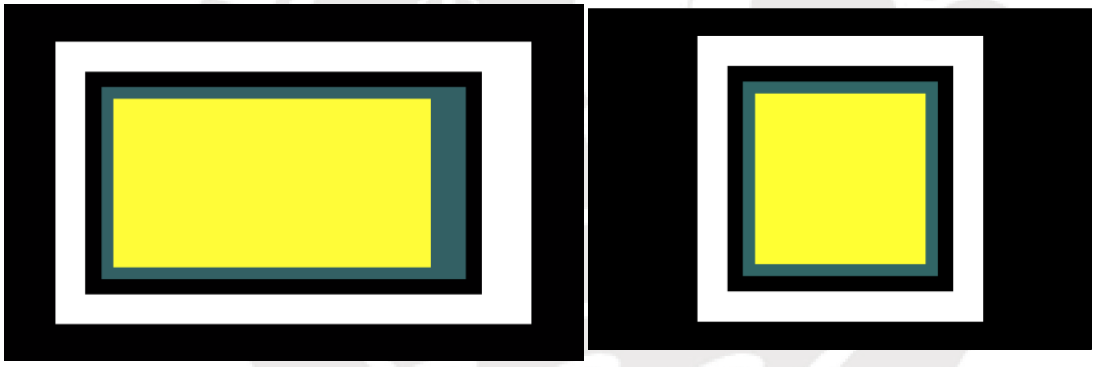

Figure 2.8: Cross section (left) and placement of front view of the complete DUNE STT detector used for simulation,showing the muon detector (white) surrounding the fiducial region and electromagnetic calorimeter

The Straw Tube Tracker DUNE ND is described in the DUNE CDR[26] and is the one we based ourselves on to create the simplified geometry we used for our simulations. For simplicity, and since most of the interactions will take place in the tracking region, we did not model interactions occuring in the nuclear targets, therefore pions were only shot in Z positions past the nuclear target region. The mass of this smaller portion of the detector was also taken into account when making calculations for the background.

Fiducial Volume This proposal for the DUNE Near Detector consists of a fiducial region of the detector that contains nuclear targets, as well as straw tube planes. The straw tube planes consist of two layers of tubes, of $1cm$ diameter, filled with a mixture of 70% Xe and 30% CO_2 gas and with a wire running through the center of the tube, making each tube a straw chamber, that detects particles based on the ionization of the gas inside it. For our geometry, each module of the detector contains two planes, of 2cm thickness each, that are of the same composition as the material inside the straw tubes described in the DUNE CDR. Each one of these planes is sandwiched between two radiator planes. Each radiator plane has approximately $9mm$ thickness and consists of 25μm planes of polypropelene (C3H6) with a 1125μm air gap between each plane. There are 80 of these modules in the detector, with a separation of $4mm$ between each module, totaling a length of $6.4m$ for the fiducial region of the detector. The total mass of the tracking region is $\sim$8 tons and the total mass of the scintillator planes, which will be the effective target of our tracking region, is of approximately 5.88 tons

Electromagnetic Calorimeter The fiducial region is surrounded by an Electromagnetic Calorimeter, which consists of lead sheets of 1.75mm thickness for the forward ECAL and of 3.5mm thickness for the barrel and backward ECALs. These between pairs of lead sheets, a layer of 10mm plastic scintillator bars were placed.

Muon Detector Both the tracking region and the electromagnetic calorimeter are expected to be surrounded by a 0.4-T dipole magnet, whose magnetic field will be usedto measure the particles momentum and charge. The return yoke of this magnet is expected to funcion as a muon spectrometer, since most particles are expected to be stopped by the thick steel walls. In order to emulate this spectrometer in our geometry we placed steel planes at the side, front and back of the detector. Inner dimensions of this steel casing is of 4m$\times$4m$\times$8m, the steel walls have a thickness of 60cm for the walls on the sides, 60cm for the front wall (upstream) and 100cm for the wall at the back (downstream).

According to the DUNE CDR, this detector will reside inside of a 0.4-T dipole magnet for the measurement of the particle momentum and charge. we have, however not simulated such magnet for our investigation. The detector is also expected to have a vertex resolution of 0.1mm and an angular resolution of 2mrad.

2.4.2.3 DUNE ND - Liquid Argon Proposal

The liquid argon proposal for the DUNE ND, as specified on the ND workshop [26], consists of several modules, each of wich is a liquid argon time projection chamber (LArTPC). Since most of the volume of the fiducial region will consist of the liquid argon used for the detection, we deemed appropriate to model this proposal with a

simple liquid argon cube if dimensions 2m 3m 5m. Since the reference does not specify an angular resolution for the detector, we took the angular resolution for the MicroBooNE LAr-TPC experiment of 3 mrad[27]. It is important to note that this detector is planned to have a magnetic field for the reconstruction of the momentums. However, we did not model that magnetic field for our simplified geometry.

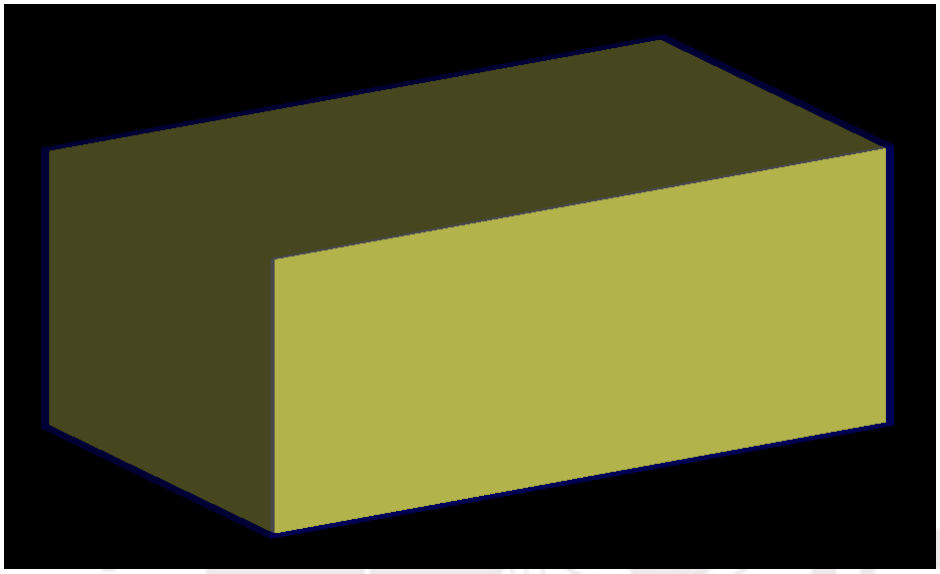

Figure 2.9: Diagram of the DUNE ND geomatry used to simulate the Liquid Argon proposal. Dimensions of the cube: 2m $\times$ 3m $\times$ 5m. Total detector mass: 25 tons.

2.5 TMVA Analysis

2.5.1 Multivariate analysis - basic deftnitions

In simple terms, Machine Learning (ML) refers to computational methods that use available information to improve performance or make accurate predictions[28]. We will begin by giving an outline of how learning algorithms work. In order to achieve this, it is necessary to first become familiar with some basic definitions.

- **Features.** Attributes associated with each element of data set, usually represented as a vector in a feature space. There characteristics can then be potentially used for the evaluation of each element. In the case of our analysis, the features we use for training are the 6 experimental observables described in table 2.1.
- **Labels.** Values or categories assigned to elements of a data set. In the case of *classification* problems, they belong to a finite set of categories e.g. In our

analysis, an events may be assigned the label of signal or background. In the case of a *regression* problems, labels are assigned real values.

- **Concept.** Given a set Λ of feature vectors and a set Ω of labels, a concept $c : \Lambda \rightarrow \Omega$ is a function that maps features $l \in \Lambda$ into the set of labels Ω.
- **Hypothesis set.** A set H of functions that map the features into the set of labels (a.k.a. concepts) from which the algorithm chooses a function $h \in H$ that is sufficiently close to the target concept c that we seek to emulate using our learning algorithm.
- **Training sample.** Example data set used to train the algorithm.
- **Test sample.** A separate data set from the training sample that is not made available during the learning stage. It represents the data the algorithm will encounter in the future, and thus is used to evaluate the performance of the learning algorithm.

Types of learning problems Multivariate analysis problems can be divided in two categories:

- **Regression.** The objective is to predict a real value for each element that is processed. E.g. predictions for stock prices, weather patterns etc. Also, since predictions arereal valued, when the quality of the algorithm is evaluated, one can define a metric for the *distance* between the predicted and real values in order do decide how much the algorithm is penalized.
- **Classiftcation.** The objective is to assign a label from a finite set of categories to each element that is processed. E.g. News stories could be classified as *sports*, *weather*, *politics*.
- **Clustering.** The objective is to partition the dataset into homogeneous regions. E.g. group paintings based oncolor palletes, identify facebook users with similar interests. Clustering is often used to analyze very large datasets[28].

2.5.2 Learning algorithms

The TMVA package provides us with a variety of learning algorithms. In order for these algorithms to *learn*, we need a **training sample**, from which the algoritm can get feedback. For example, if one were to design an algorithm that pursued to learn how to play chess, the training sample could consist of a set of past games, that the algorithm may use to guide its learning process. Depending on the type of feedback the algorith gets form its training sample, the learning process may be classified into three types[29].

- **Unsupervised Learning.** No feedback is given to the algorithm, nonetheless, it derives patterns from the *features* of elements in the training dataset. Using the example above, a learning algorithm could receive a set of chess games played by different players and cluster together games with similar playing patterns.

- **Reinforcement Learing.** The algorithm learns from a series of rewards and punishments, however, it does not know the direct relationship between the reinforcements and the behavior that caused them. An example of this, in the context of the chess algorithm, could be if it did not receive any feedback on the quality of its moves, but instead altered its playing patterns based on which games resulted in a win or a loss.

- **Supervised Learning.** Information is already known about the desired classification of the training data set. Then, the algorithm trains to try to increase the positive feedback it receives. In the context of chess algorithm, this would be equivalent to the algorithm receiving feedback on the quality of the moves it chooses, as well as from the end result of the games, based on the past games from the training dataset.

In the case of our investigation, we have considered two algorithms for supervised learning in order to solve the classification problem of distinguishing the signal from background. After considering the different quantities that can be observed by the detector, along with the fact that the signal of the trident process is characterized by a $\mu^+\mu$ pair coming from the vertex, we defined six different experimental observables, detailed in Table 2.1. Once with these observables in mind, we tested two multi-variate analysis (MVA) classification techniques, offered by the ROOT TMVA Package. Since the relacionship between the variables not linear, we deemed it interesting to compare a linear method, like Boosted Decision Trees (BDTs), and a non-linear one, like k-Nearest Neighbors (kNN).

In the following section, we proceed to describe these different methods, how they are trained, and how they treat multi-dimensional space, in order to select the signal.

2.5.2.1 Boosted Decision Trees (BDT)

Classiftcation Trees Decision trees can be used to solve either classification or regression problems. When the tree is used to classify data, it is called a *classification tree*. The treatment of the multi-dimensional variable space by a decision tree (DT), is based on making cuts on the different variables available. At each stage of the tree training, a cut in one of the variables is made creating an extra subregion of the variable space. The variable on which the cut is made, as well as the value of the cut, can be determined by differente criteria. In the case of our investigation, we used the Gini Index, which measures the homogeneity of data in a subregion and is defined as

$G = p(1\ p)$ where p is the purity of a region in the variable space. In our case, if events can be classified only as *signal* or *background* events, the purity is calculated as $p = S/(S+B)$, where S and B are the number of signal and background events, respectively. Figure 2.10 shows an example ofdecision tree bein trained in atwo-dimensional variable space, where at steps t1, t2 and t3 cuts are progessively made, ending up with dividing the variable space in subregions R3, R4, R5 and R6.

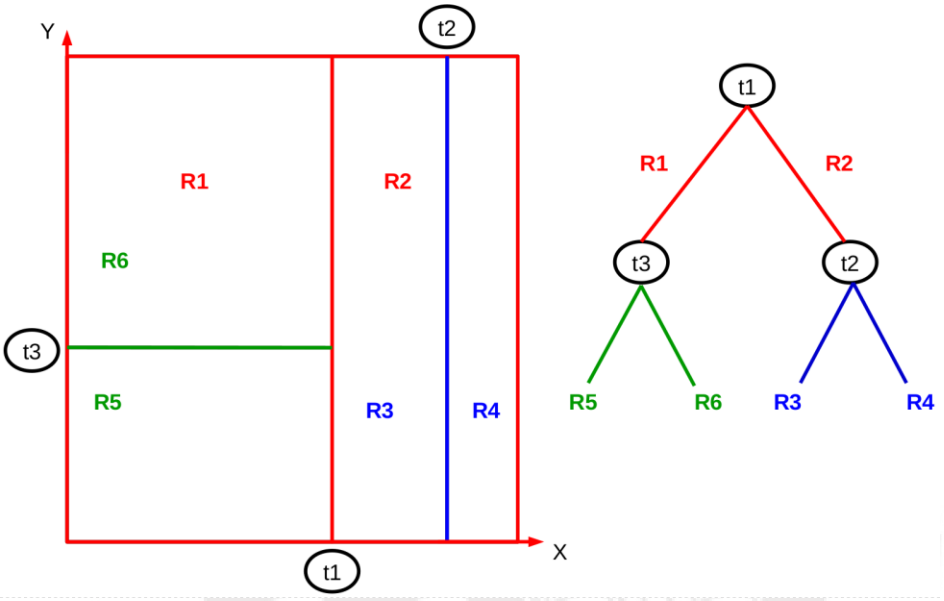

Figure 2.10: Description of signal selection for Boosted Decision Trees

Boosting In order to increase the speed and improve the predictions of a DT, one can use *Ensemble methods*. Ensemble method consist on combining several inefficient predictor that combine one can add extra steps into the tree making algorithms, these methods are called "Boosting". The type of boosting chosen for our analysis is *adaptive boosting* (AdaBoost). Adaptive boosting consists of making a many DT's with thesame data set, but each time adding an additional weight α to the data that is misclassified. The weight α that is applied on an event depends on the misclassification rate (err) of the previous tree.

$$\alpha = \frac{1 - err}{err} \tag{2.1}$$

The output of each of these classification trees is defined as $h(\mathbf{x})$, where $\mathbf{x}$ is the ntuple of variables corresponding to an event, and yelds +1 for signal events and -1 for background events. The combined output is calculated by adding the $h(\mathbf{x})$ in the following manner:

$$y_{boost}(\mathbf{x}) = \frac{1}{N} \sum_{i} ln(\alpha_i) h_i(\mathbf{x}) \quad (2.2)$$

Where the $h_i(\mathbf{x})$ is the output of the ith event, and N is the total number of trained trees. The idea behind the concept of adaptive boosting is to guide the algorithm into making cuts that favour the selection of more difficul-to-classify data points, and adding the output of weak classifiers (Decision Trees) into a strongclassifier.

2.5.2.2 k-Nearest Neighbors (kNN)

The k-Nearest Neighbor algorithm selection process is ordered in the following way:

1. Training phase. The **training sample** is read and, for each data point, the information of whether it is a signal or background event is stored.
2. An appropriate metric is chosen in order to judge the "distance" between data points, e.g. Euclidian distance, in case the variables lie in a continuous space.
3. Classification Phase. The **test sample** is taken and, for each datapoint, the k datapoints from the **training sample** that are "nearest" to it, based on the metric chosen, are selected. Then, the data point form the test sample is classified based on the most common classification (signal or background) among those 7 data points.

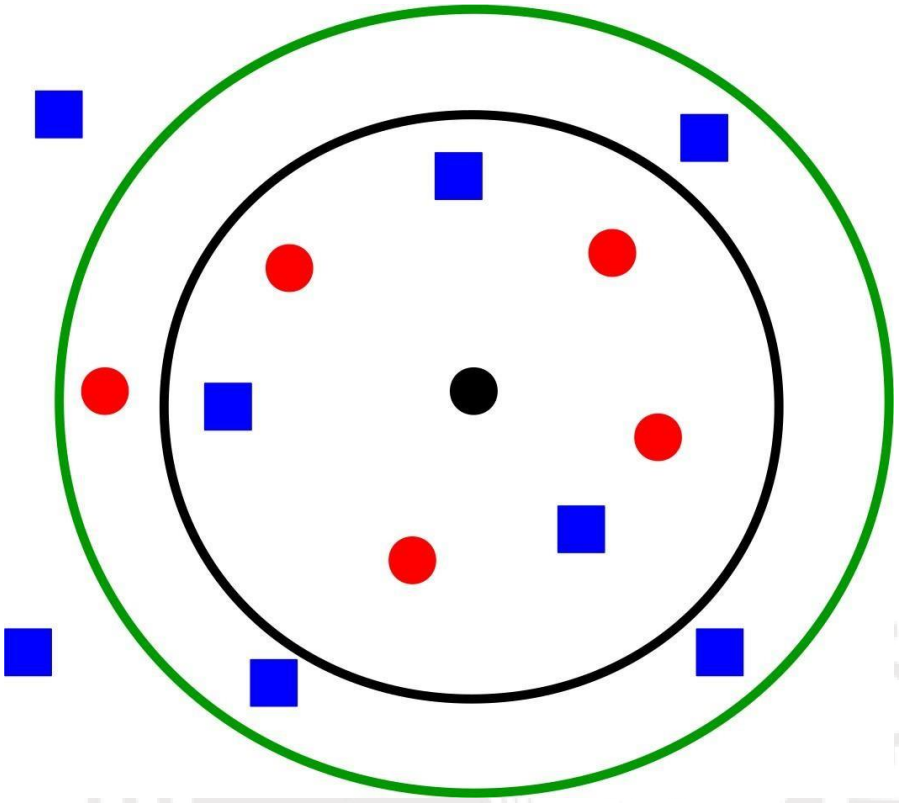

Figure 2.11: Description of signal selection for k-Nearest Neighbors

For the weights that we used in the TMVA analysis were the expected number of events for trident and background signals in the for the different experiment fluxes. These event rates were calculated by convolution of the calculated cross sections with the fluxes portrayed in figure 2.5. The detailed calculations of the expected number of events for the backgrounds are shown in appendix B.

Chapter 3

Results

In the following section, we proceed report the results of the analysis made for the different detector geometries and beam configurations. The order is as follows: First, we report the results from our background simulation for the pion backgrounds (contained pions and passed pions). Then, the significance results for the MINERνA-like detector are presented, for both the NuMI ME and HE beam configurations. Finally, the results for the DUNE-ND-like detectors are presented, for the STT and LArTPC proposals. In this case we considered two dofferent experimental exposures to present our DUNE ND results. The first set of results assume a 850 kT-MW-yr exposure in DUNE's lifetime, as it was assumed by Magill[5]. The second exposure assumed is of 300 kT-MW-yr, corresponding to the DUNE experiment running for 7 years, with a 40kT far detector and a 1.04MW reference beam.

3.1 Pion background results

After π^+ were shot inside of the detector, one of three things could happen to them: they could go through the entire detector, in which case they would be added to the **passed pions** background, they could undergo a **DIS** interaction with the material of the detector, or finally, they could decay and produce a μ^+ and a ν_μ. Tables 3.1 and 3.2 shows the rate at which the pion did one of these three things inside of the detector, for coherent and incoherent interactions respectively. The fourth row in the table shows the percentage of the decayed pions that are eligible as **contained pion** backgrounds. As described in section 1, this would mean that the angle the μ^+ arising from the decay forms with the track of its parent π^+ is smaller than the detector's angular resolution. As a reminder, the angular resolution for the MINERνA detector's fiducial region is of 0.5^o, the angular resolution of the DUNE STT Dear Detector is of 2mrad (0.115^o) and for the DUNELArTPC proposal, wehavetaken the MicroBOONE's angular resolution of 3mrad (0.17^o).

Interaction \Detector	DUNE STT	DUNE ARGON	MINERvA-like ME	MINERvA-like pHE
Passed Pions	15.20%	12.43%	3.12%	3.00%
DIS Pions	65.33%	74.16%	84.39%	85.65%
Decayed Pions	19.47%	13.41%	12.49%	11.37%
Contained Pions (% of Decayed Pions)	0.03%	0.026%	0.39%	0.51%

Table 3.1: Distribution of interactions of Pions inside of each detector for **coherent interactions**. **NOTE:** Angular resolution of 2mrad was used for the DUNE STT and of 3 mrad for the DUNE Argon detector, based on the Microboone angular resolution[27].

Interaction	DUNE STT	DUNE ARGON	MINERvA-like ME	MINERvA-like pHE
Passed Pions	21.77%	10.97%	3.78%	3.67%
DIS Pions	52.03%	70.39%	77.30%	78.84%
Decayed Pions	26.20%	18.64%	18.92%	17.48%
Contained Pions (% of Decayed Pions)	0.017%	0.016%	0.20%	0.26%
Coh π^{0}'s	5.46%	5.34%	6.6%	7.82%
Protons in FS	34.41%	22.02%	26.04%	24.35%
Neutrons in FS	60.13%	72.64%	67.36%	67.83%

Table 3.2: Distribution of interactions of Pions inside of each detector for **incoherent interactions**

3.2 Significance results

Then, after running our TMVA analysis, we were able to obtain signal and background efficiencies, as well as the significance for the coherent and incoheren processes. First we proceed to compare the effectiveness of the two TMVA methods used. It should be noted that the formula used by TMVA to calculate the significance is:

$$S = \frac{S}{\sqrt{S+B}} \tag{3.1}$$

The MINERνA-like detector

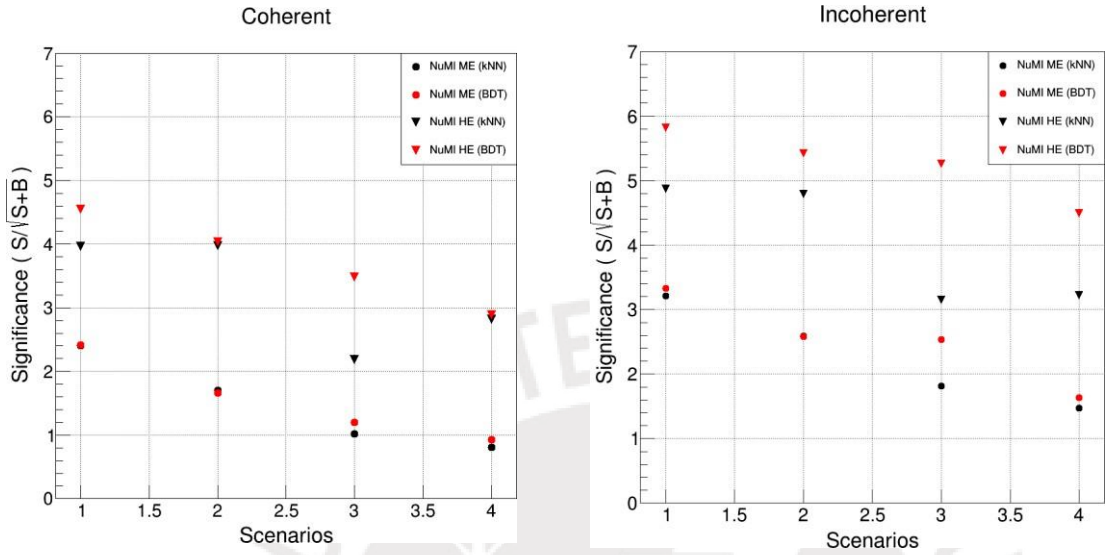

Figure 3.1: Significance results for NuMI ME and NuMI pHE beams in a MINERνA-like geometry

The DUNE Near Detector assuming a 850 kT-MW-yr exposure

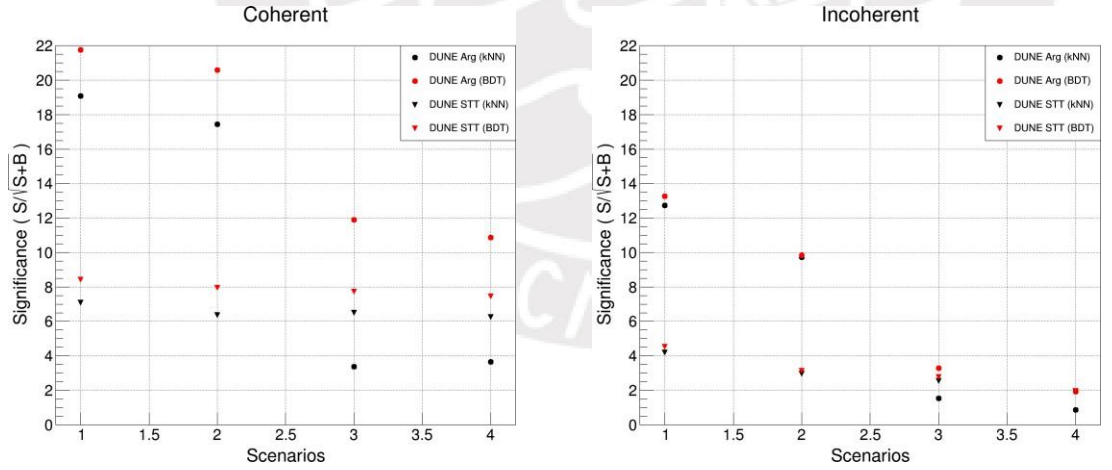

Figure 3.2: Significance plots for the Liquid Argon, and STT proposals for the DUNE Near Detector

If we compare both DUNE scenarios shown in figure 3.2, we can see that the DUNE LArTPC detector suffers a steep loss in significances in scenarios 3 and 4, compared to

1 and 2. To understand this, we need to note that, as noted in section 2.1, cases 3 and 4 differ from cases 1 and 2 in that they take in to account an aditional background: *passed pions*. The passed pions background is very numerous for the DUNE LArTPC detector because there is no aditional calorimetry to constrain the π^+'s coming from interactions inside of the detector.

As it can be seen in figure 3.2, the significance for the DUNE Argon proposal is much larger than that of the STT detector. This makes sense, because the argon detector is much more massive, 25 tons compared to 5.88 tons of the DUNE STT detector. Even though the detector will also have a larger background, if one looks at the equation for the significance above, it is evident that is the signal increases at the same rate as the background, then the significance is expected to increase, due to the square root in the denomitator. One can even notice that, as seen in Appendix B, the *passed pions* background is much larger for the DUNE Argon detector, not only because of the detector size, but also because its lack of calorimetry, however, the increase in the signal had such an important effect, that even for cases 3 and 4 the DUNE Argon detector still shows greater significance values than the DUNE STT detector, when using the BDT method.

The DUNE-like geometry (Exposure 300 kT-MW-yr)

Now we proceed to present the same significance plots as in figure 3.2, but calculated for an exposure of 300 kT-MW-yr. They show the same trends as the previous section, however the significances are more comparable to those for the MINERνA-like detectors.

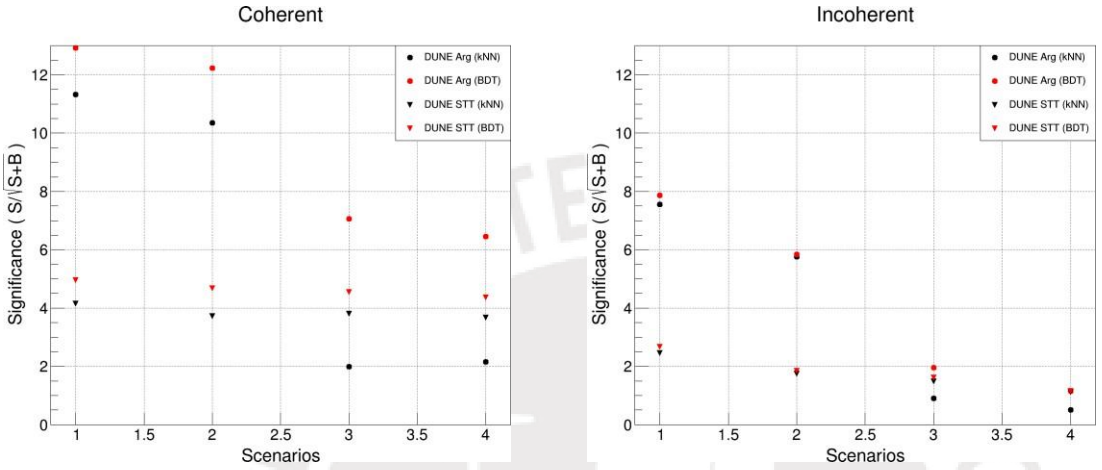

Figure 3.3: Significance plots for the Liquid Argon, and STT proposals for the DUNE Near Detector

Seeing as the BDT method was the most effective one to separate the signal from the background, it was the one chosen to fill the tables that report the significances for the coherent (Tables 3.3 and 3.6) as well as the incoherent (Tables 3.4 and 3.7) cases. Finally, we considered that protons and neutrons are not always visible to a detector, especially if they have low energy. This puts into question, if it really makes sense to assume that a detector will always be able to distinguish between a coherent and an incoherent trident interaction. Thus, we considered interesting to repeat the TMVA analysis, but this time the combination of the coherent and incoherent processes as the signal. Since the background signal for the coherent process is completely contained inside of the background signal for the incoherent process, for this new analysis the background signal remained the same as for the incoherent case. The results are shown in tables 3.5 and 3.8 below.

3.3 Conclusions and prospects for future investigations

Theoretical crosschecks and extensions First, we were able to recleate the calculations by references [11] and [7], to the point that we were able to extend these

calculations to the SM by adding the effecto of the C_V and C_A couplings. Although these new calculations have not yet been implemented in GENIE, this is a direction that the investigation could take in te future. However, it should be noted that the expressions that are shown in appendix A, although really long, have been calculated for the case in which both muons in the final state dimuon pair are of the same flavor. If we were to consider dimuon pairs of different flavors, then the calculated expressions would be much larger. Therefore, it would be helpful to study which approximations would be appropriate to reduce these expressions in size, in order to make it more feasible to add them into the GENIE generator objects.

Signal simulation Thetrident production process has been successfully implemented in the GENIE montecarlo generator, for both the coherent and incoherent processes. Although the full calculations taking into account the C_V and C_A directly from the cross section calculation have been made, for the purpose of this investigation, the cross-section that was implemented in GENIE was the one calculated in the V-A theory, like the one calculated in reference [7] to which we applied a correction factor based on the one used by reference [4], in order to compensate for the effect of the interference between NC and CC bosons. This could be done because this investigation concentrated on the analysis of the dimuon case of trident production, which is the same context in which Altmannshofer used this approximation. Finally, we were able to successfully generate weighted trident prodcution events in the GENIE montecarlo, for both the coherent and incoherent scenarios. Future plans include using the results on A to implement the full SM cross-section in GENIE.

Background simulation We were able to construct Geant4 geometries that could closely emulate the MINERvA detector and as well as tentative DUNE ND proposals, namely the STT and the LArTPC proposals. These geometries were then used to simulate the behaviour of π^+s inside ofthe detector, in ordertosee at which proportion they would interact, decay, or go through the detector and escape. Could then use this information to get the proportions that we could expect of the background events coming from the contained pions and passed pions as described in section 1.4. We also generated a sufficient amount of charm production events, in order to discern which charmed particles could cause a dimuon background that would be relevant to our investigation. The conclusion was that, given the cuts that we will apply to our signal regarding the number of particles that are expected to come out of an interaction vertex, the only charmed particle whose decay could be considered background, would be the λ_c^+. It should be noted, that this charm production evetn would coluld only be a potential background for coherent trident production if the neutron produced were not to be detected. However, since this depends mucho on the reconstruction techniques of each detectorteam, wedeemed it appropriate to assume that the neutron

is always invisibleto the detector, in order to give a worst case scenario estimate for the background.

TMVA analysis As it is portrayed on the result tables below, the TMVA based on the DUNE ND proposals have resulted in large significances, for both the 300 kT-MW-yr and the 500 kT-MW-yr exposures. Even the predictions based on the NuMI beamline have shown promising significances of around 4 σ's. This allows us to conclude that, based on the analysis made by this investigation which has taken into account three types of background, as well as the coherent and incoherent trident processes, it is possible to make an excellent distinction between the trident signal from its background processes based on the variable we defined for our TMVA analysis. Furthermore, predictions on the number of events expected in the DUNE ND lifetime is very high. We are therefore able to conclude that it is feasible to pursue the measurement of trident production in the future DUNE ND, as well as the MINERνA detector, in case the high energy NuMI beam were to be put into operation.

3.4 Summary Tables

From the result tables one can conclude that there are two main factor that should be taken in to account when determining whether an experiment is feasible for detecting trident production events: Detector size and appropriate muon detection, which usually implies the use of an effective calorimeter, as those shown in figures 2.6 and 2.8 for the MINERvA and DUNE STT Near Detector respectively. However, it is also important to note that the Liquid argon proposal shows a greater significance even when their background signal is much higher, as shown in appendix B. The reason being that the detector size (25 tons) is large enough for it to have a large enough signal that allows the BDT algorith to make much stricter while maintaining a good signal/background ratio.

	DUNE Arg			DUNE Scint		
Case	**Signal**	**Backg.**	**Signif.**	**Signal**	**Backg.**	**Signif.**
1	490	17	21.760	73	3	8.412
2	447	24	20.595	69	7	7.942
3	231	147	11.899	74	18	7.719
4	118	0	10.867	72	22	7.421
	NuMI ME			**NuMI HE**		
Case	**Signal**	**Backg.**	**Signif.**	**Signal**	**Backg.**	**Signif.**
1	11	10	2.414	21	1	4.525
2	5	5	1.662	19	4	4.029
3	6	24	1.199	18	10	3.449
4	4	18	0.932	16	15	2.887

Table 3.3: Expected number of signal events (Sgn), Background events (Bkg), and Significance (measured in σ's) for the four detector designs considered for the **coherent case** assuming a 850 kT-MW-yr exposure.

	DUNE Arg			DUNE Scint		
Case	**Signal**	**Backg.**	**Signif.**	**Signal**	**Backg.**	**Signif.**
1	321	268	13.245	45	56	4.522
2	540	2483	9.829	39	123	3.128
3	15	6	3.288	52	308	2.753
4	7	6	1.927	94	2236	1.955
	NuMI ME			**NuMI HE**		
Case	**Signal**	**Backg.**	**Signif.**	**Signal**	**Backg.**	**Signif.**
1	6	7	1.676	14	2	3.520
2	4	5	1.305	13	4	3.111
3	5	11	1.266	14	10	2.930
4	1	0	0.812	11	10	2.428

Table 3.4: Expected number of signal events (Sgn), Background events (Bkg), and Significance (measured in σ's) for the four detector designs considered for the **incoherent case** assuming a 850 kT-MW-yr exposure.

	DUNE Arg			DUNE Scint		
Case	**Signal**	**Backg.**	**Signif.**	**Signal**	**Backg.**	**Signif.**
1	838	33	28.386	125	10	10.743
2	793	75	26.912	114	14	10.079
3	341	0	18.443	119	34	9.655
4	215	1	14.630	107	41	8.806
	NuMI ME			**NuMI HE**		
Case	**Signal**	**Backg.**	**Signif.**	**Signal**	**Backg.**	**Signif.**
1	19	15	3.226	37	3	5.794
2	11	7	2.495	36	8	5.376
3	12	11	2.511	35	10	5.259
4	6	9	1.612	27	10	4.488

Table 3.5: Expected number of signal events (Sgn), Background events (Bkg), and Significance (measured in σ's) for the four detector designs considered for an inclusive signal that includes the **coherent and incoherent** cases assuming a 850 kT-MW-yr exposure.

	DUNE Arg			DUNE Scint		
Case	**Signal**	**Backg.**	**Signif.**	**Signal**	**Backg.**	**Signif.**
1	172	6	12.921	25	1	4.948
2	157	8	12.229	24	2	4.669
3	81	51	7.065	25	6	4.533
4	41	0	6.453	24	7	4.357
	NuMI ME			**NuMI HE**		
Case	**Signal**	**Backg.**	**Signif.**	**Signal**	**Backg.**	**Signif.**
1	11	10	2.414	21	1	4.525
2	5	5	1.662	19	4	4.029
3	6	24	1.199	18	10	3.449
4	4	18	0.932	16	15	2.887

Table 3.6: Expected number of signal events (Sgn), Background events (Bkg), and Significance (measured in σ's) for the four detector designs considered for the **coherent case** assuming a 300 kT-MW-yr exposure.

	DUNE Arg			DUNE Scint		
Case	**Signal**	**Backg.**	**Signif.**	**Signal**	**Backg.**	**Signif.**
1	34	36	4.086	5	9	1.322
2	53	371	2.581	3	11	0.848
3	2	2	1.046	3	23	0.724
4	1	2	0.567	13	788	0.480
	NuMI ME			**NuMI HE**		
Case	**Signal**	**Backg.**	**Signif.**	**Signal**	**Backg.**	**Signif.**
1	6	7	1.676	14	2	3.520
2	4	5	1.305	13	4	3.111
3	5	11	1.266	14	10	2.930
4	1	0	0.812	11	10	2.428

Table 3.7: Expected number of signal events (Sgn), Background events (Bkg), and Significance (measured in σ's) for the four detector designs considered for the **incoherent case** assuming a 300 kT-MW-yr exposure.

	DUNE Arg			DUNE Scint		
Case	**Signal**	**Backg.**	**Signif.**	**Signal**	**Backg.**	**Signif.**
1	295	8	16.942	43	2	6.450
2	279	19	16.169	41	4	6.129
3	120	0	10.949	41	10	5.805
4	76	0	8.686	39	14	5.331
	NuMI ME			**NuMI HE**		
Case	**Signal**	**Backg.**	**Signif.**	**Signal**	**Backg.**	**Signif.**
1	19	15	3.226	37	3	5.794
2	11	7	2.495	36	8	5.376
3	12	11	2.511	35	10	5.259
4	6	9	1.612	27	10	4.488

Table 3.8: Expected number of signal events (Sgn), Background events (Bkg), and Significance (measured in σ's) for the four detector designs considered for an inclusive signal that includes the **coherent and incoherent** cases assuming a 300 kT-MW-yr exposure.

Appendix A

Calculated traces of for the SM

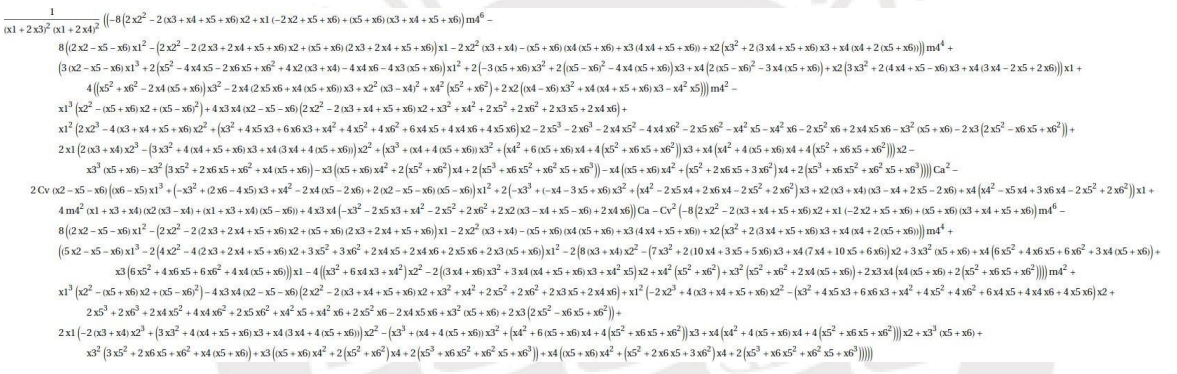

Figure A.1: $P_\mu L_{\mu\nu} P_\nu$ reduction

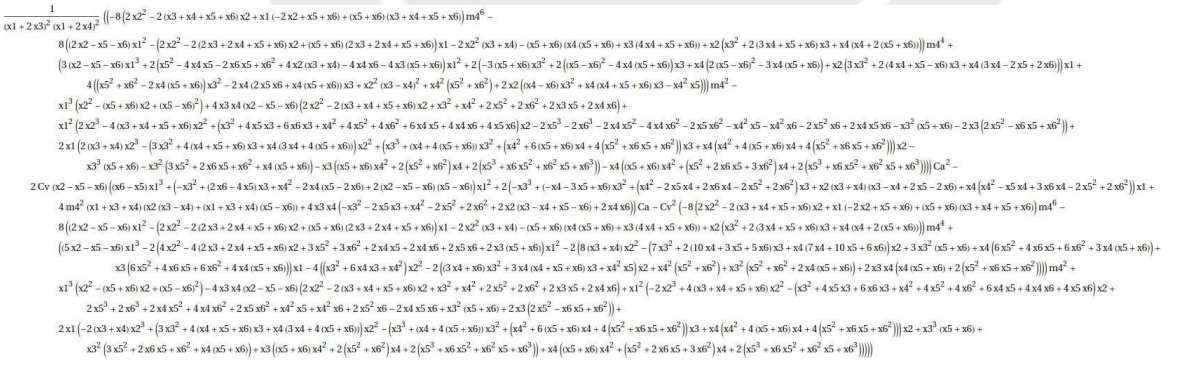

Figure A.2: $L_{\mu\nu}\delta_{\mu\nu}$ reduction

Figure A.3

Appendix B

Calculation of Weights for TMVA analysis

In this section, I give the details of how the weights have been calculated for the TMVA analysis

Amount of Pions expected in each experiment
For the **coherent** case:
For NuMI ME:
Calculated from GENIE generation:

- For every 12e6 events, we have 857973 Pions **7.148**%

For NuM HE:
Calculated from GENIE generation:

- For every 12e6 events, we have 1499669 Pions **5.735**%

For DUNE STT:
Calculated from GENIE generation:

- For every 156.221e6 events, we have 8345751 Pions **5.342**%

For DUNE Argon:
Calculated from GENIE generation:

- For every 171.057e6 events, we have 8783086 Pions **5.134**%

Interaction \Detector	DUNE STT	DUNE ARGON	MINERvA-like ME	MINERvA-like pHE
Passed Pions	15.20%	12.43%	3.12%	3.00%
DIS Pions	65.33%	74.16%	84.39%	85.65%
Decayed Pions	19.47%	13.41%	12.49%	11.37%
Contained Pions (% of Decayed Pions)	0.03%	0.026%	0.39%	0.51%

Table B.1: Distribution of interactions of Pions inside of each detector for **coherent interactions**. **NOTE:** Angular resolution of 2mrad was used for the DUNE STT and of 3mrad for the DUNE Argon detector, based on the Microboone angular resolution[27].

Interaction \Detector	DUNE STT	DUNE ARGON	MINERvA-like ME	MINERvA-like pHE
Expected # of events	27600000	144423900	20460400	22797733
Expected # of CC events	20400000	106748100	15345300	17098300
Expected # of Bg Pions	1474392	7414723	1462509	1307450
Passed Pions	224107	921650	45630	39224
Contained Pions (% of Decayed Pions)	86	259	712	758
Charm Production	134	810	146	131
Trident	12	92	15	23

Table B.2: Calculated weights for **coherent interactions**

For the **incoherent** case:
For NuMI ME: Calculated from GENIE generation:

- For every 12e6 events, we have 857973 Pions **12.497**%

For NuMI HE: Calculated from GENIE generation:

- For every 12e6 events, we have 1499669 Pions **9.670**%

For DUNE STT:
Calculated from GENIE generation:

- For every 15e6 events, we have 2229215 Pions **14.861**%

For DUNE Argon:
Calculated from GENIE generation:

- For every 12e6 events, we have 1018645 Pions **8.489**%

Interaction	DUNE STT	DUNE ARGON	MINERvA-like ME	MINERvA-like pHE
Passed Pions	21.77%	10.97%	3.78%	3.67%
DIS Pions	52.03%	70.39%	77.30%	78.84%
Decayed Pions	26.20%	18.64%	18.92%	17.48%
Contained Pions (% of Decayed Pions)	0.017%	0.016%	0.20%	0.26%
Coh π^{0}'s	5.46%	5.34%	6.6%	7.82%
Protons in FS	34.41%	22.02%	26.04%	24.35%
Neutrons in FS	60.13%	72.64%	67.36%	67.83%

Table B.3: Distribution of interactions of Pions inside of each detector for **incoherent interactions**

Interaction \Detector	DUNE STT	DUNE ARGON	MINERvA-like ME	MINERvA-like pHE
Expected # of events	27600000	144423900	20460400	22797733
Expected # of CC events	20400000	106748100	15345300	17098300
Expected # of Bg Pions	4101636	12260145	2556936	2204541
Passed Pions	550029	1344938	96653	80907
Contained Pions (% of Decayed Pions)	202	366	968	1002
Charm Production	134	810	146	131
Trident	9	65	11	16

Table B.4: Calculated weights for **incoherent interactions**

Interaction	DUNE STT	DUNE ARGON	MINERvA-like ME	MINERvA-like pHE
Passed Pions	0.02%	10.97%	3.78%	3.67%
DIS Pions	68.59%	70.39%	77.30%	78.84%
Decayed Pions	31.39%	18.64%	18.92%	17.48%
Contained Pions (% of Decayed Pions)	0.015%	0.016%	0.20%	0.26%
Coh π^{0}'s	5.46%	5.34%	6.6%	7.82%
Protons in FS	34.41%	22.02%	26.04%	24.35%
Neutrons in FS	60.13%	72.64%	67.36%	67.83%

Table B.5: Distribution of interactions of Pions inside of each detector for **incoherent interactions** using a **Hadronic calorimeter for the DUNE STT detector**

Interaction \Detector	DUNE STT	DUNE ARGON	MINERvA-like ME	MINERvA-like pHE
Expected # of events	27600000	144423900	20460400	22797733
Expected # of CC events	20400000	106748100	15345300	17098300
Expected # of Bg Pions	4101636	12260145	2556936	2204541
Passed Pions	821	1344938	96653	80907
Contained Pions (% of Decayed Pions)	194	366	968	1002
Charm Production	134	810	146	131
Trident	9	65	11	16

Table B.6: Calculated weights for **incoherent interactions** using a **Hadronic calorimeter for the DUNE STT detector**

Bibliography

[1] J. M. Paley. Recent results and future prospects for MINOS. 2009.

[2] C. Mariani. Recent results from K2K experiment. 2005.

[3] J. A. Formaggio and G. P. Zeller. From ev to eev: Neutrino cross sections across energy scales. *Rev. Mod. Phys.*, 84:1307–1341, Sep 2012.

[4] Wolfgang Altmannshofer, Stefania Gori, Maxim Pospelov, and Itay Yavin. Neutrino Trident Production: A Powerful Probe of New Physics with Neutrino Beams. *Phys. Rev. Lett.*, 113:091801, 2014.

[5] Gabriel Magill and Ryan Plestid. Neutrino Trident Production at the Intensity Frontier. *Phys. Rev.*, D95(7):073004, 2017.

[6] T. Adams et al. Evidence for diffractive charm production in muon-neutrino Fe and anti-muon-neutrino Fe scattering at the Tevatron. *Phys. Rev.*, D61:092001, 2000.

[7] J. Lovseth and M. Radomiski. Kinematical distributions of neutrino-produced lepton triplets. *Phys. Rev.*, D3:2686–2706, 1971.

[8] Andreas Hoecker, Peter Speckmayer, Joerg Stelzer, Jan Therhaag, Eckhard von Toerne, and Helge Voss. TMVA: Toolkit for Multivariate Data Analysis. *PoS*, ACAT:040, 2007.

[9] D. Geiregat et al. First observation of neutrino trident production. *Phys. Lett.*, B245:271–275, 1990.

[10] T. Adams et al. Neutrino trident production from NuTeV. In *High-energy physics. Proceedings, 29th International Conference, ICHEP'98, Vancouver, Canada, July 23-29, 1998. Vol. 1, 2*, pages 631–634, 1998.

[11] W. Czyz, G. C. Sheppey, and J. D. Walecka. Neutrino production of lepton pairs through the point four-fermion interaction. *Nuovo Cim.*, 34:404–435, 1964.

[12] David Griffiths. *Introduction to elementary particles*. WILEY-VCH Verlag GmbH & Co. KGaA, Weinheim, 2004.

[13] Vladyslav Shtabovenko, Rolf Mertig, and Frederik Orellana. New Developments in FeynCalc 9.0. *Comput. Phys. Commun.*, 207:432–444, 2016.

[14] Herbert Überall. *Electron Scattering from Complex Nuclei Part A*. Academic Press, New york, 1971.

[15] H. De Vries, C. W. De Jager, and C. De Vries. Nuclear charge density distribution parameters from elastic electron scattering. *Atom. Data Nucl. Data Tabl.*, 36:495–536, 1987.

[16] P.L. Hallowell J.T. O'Brien S. Penner J.M. Finn, Hall Crannell. Elastic electron scattering from the isotopes ^{36}Ar and 40Ar. *Phys. Rev.*, A274:28–44, 1976.

[17] R. W. Brown, R. H. Hobbs, J. Smith, and N. Stanko. Intermediate boson. iii. virtual-boson effects in neutrino trident production. *Phys. Rev.*, D6:3273–3292, 1972.

[18] S. Agostinelli et al. GEANT4: A Simulation toolkit. *Nucl. Instrum. Meth.*, A506:250–303, 2003.

[19] R. Acciarri et al. Long-Baseline Neutrino Facility (LBNF) and Deep Underground Neutrino Experiment (DUNE). 2016.

[20] Melissa T Jerkins, SK Singh, JG Morfin, Makoto Sakuda, and KD Purohit. Measuring the numi beam flux for minerva. In *AIP Conference Proceedings*, volume 1405, pages 362–367. AIP, 2011.

[21] T. Alion et al. Experiment Simulation ConfigurationsUsed in DUNE CDR. 2016.

[22] Bipul Bhuyan. High Resolution Fine-Grained Tracker: Reference Near Detector for DUNE. 2017.

[23] James Sinclair. High Resolution Fine-Grained Tracker: Reference Near Detector for DUNE. 2017.

[24] P. Adamson et al. The NuMI Neutrino Beam. *Nucl. Instrum. Meth.*, A806:279–306, 2016.

[25] L. Aliaga et al. Design, Calibration, and Performance of the MINERvA Detector. *Nucl. Instrum. Meth.*, A743:130–159, 2014.

[26] R. Acciarri et al. Long-Baseline Neutrino Facility (LBNF) and Deep Underground Neutrino Experiment (DUNE). 2016.

[27] P. Abratenko. Determination of muon momentum in the MicroBooNE LArTPC using an improved model of multiple Coulomb scattering. 2017. [J. Phys. Conf. Ser.408,012039(2013)].

[28] Afshin Rostamizadeh Mehryar Mohri and Ameet Talwalkar. *Foundations of Machine Learning*. MIT Press, Cambridge, Massachusetts, 2012.

[29] Stuart Russell and Norvig Peter. *Artificial Intelligence: A Modern Approach*. Prentice Hall, New Jersey, 2010.